Development of a Numerical Model of High-Intensity Focused Ultrasound Treatment in Mobile and Elastic Organs: Application to a Beating Heart

Elodie Cao, Paul Greillier, Raphaël Loyet, Françoise Chavrier, Jade Robert, Francis Bessière, Jean-Louis Dillenseger, Cyril Lafon

Development of a numerical model of HIFU treatment in mobile and elastic organs: Application to a beating heart

Elodie Cao[a,*], Paul Greillier[a], Raphaël Loyet[a], Françoise Chavrier[a], Jade Robert[a], Francis Bessière[a,b], Jean-Louis Dillenseger[c], Cyril Lafon[a]

[a] LabTAU, INSERM, Centre Léon Bérard, Université Lyon 1, Univ Lyon, F-69003 Lyon, France

[b] Hospices Civils de Lyon, Hôpital Cardiovasculaire Louis Pradel, Lyon, France

[c] Univ Rennes, Inserm, LTSI - UMR 1099, F-35000 Rennes, France

* Corresponding author – 151 cours Albert Thomas, 69003 Lyon – elodie.cao@inserm.fr – Phone number : +33649234979

Abstract

High-intensity focused ultrasound (HIFU) is a promising method to treat cardiac arrhythmias, as it can induce lesions at a distance throughout myocardium thickness. Numerical modeling is commonly used for ultrasound probe development and optimization of HIFU treatment strategies. This study aims to describe a numerical method to simulate HIFU thermal ablation in elastic and mobile heart models. The ultrasound pressure field is computed on a 3-dimensional (3D) orthonormal grid using the Rayleigh integral method, and the attenuation is calculated step by step between cells. The temperature distribution is obtained by the resolution of the BioHeat Transfer Equation (BHTE) on a 3D nonorthogonally structured curvilinear grid using the finite volume method. The simulation method is applied on two regions of the heart (atrioventricular node and ventricular apex) to compare the thermal effects of HIFU ablation depending on deformation, motion type and amplitude. The atrioventricular node requires longer sonication than the ventricular apex to reach the same lesion volume. Motion considerably influences treatment duration, lesion shape, and distribution in cardiac HIFU treatment. These results emphasize the importance of considering local motion and deformation in numerical studies to define efficient and accurate treatment strategies.

Keywords: high-intensity focused ultrasound, cardiac applications, mobile organs, bioheat transfer equation, curvilinear grid, finite volume method

Introduction

Cardiovascular diseases (CVDs) are the leading cause of mortality worldwide, with more than twice the number of cancer-related deaths (Roth et al. 2018). Cardiac arrhythmias (CAs) are CVDs originating from an electrical dysfunction in the heart conduction pathway, which leads to abnormal heartbeat. While atrial fibrillation is the most common CA (Timmis et al. 2018), ventricular tachycardia presents the greatest risk of sudden death (Harris and Lysitsas 2016). In clinical routine, these pathologies are treated by thermal ablation of arrhythmogenic foci or reentrant circuits using a radiofrequency catheter. This technique remains invasive and has a recurrence rate of 30% to 50% (Tung et al. 2015).

High-intensity focused ultrasound (HIFU) is clinically used in the treatment of several pathologies, such as prostate cancer (Gelet et al. 2000), uterine fibroids (Ji et al. 2017), and essential tremors (Park et al. 2019). HIFU enables fast and precise ablation during non or minimally invasive procedures and has been proposed as an alternative therapy to treat CAs. The transesophageal approach has been studied because it offers an excellent acoustic window, and the proof of concept has been presented *in silico* (Constanciel et al. 2013; Pichardo and Hynynen 2009), *in vitro* (Constanciel et al. 2013) and *in vivo* in swine (Bessiere et al. 2016). *Ex vivo* experiments on beating heart models have demonstrated the ability to produce thermal lesions with a transesophageal probe in mobile organs. However, further *in vivo* experiments on baboons have emphasized difficulties caused by heart motion (Greillier et al. 2018). Consequently, it clearly appears that more accurate simulation tools are required to precisely predict the position and shape of HIFU lesions on the beating heart.

Numerical modeling is currently used during the early phases of the design of HIFU probes, and has contributed to the design of innovative transducer geometry in response to medical needs (Bawiec et al. 2018; Charrel et al. 2011; Curiel et al. 2002). Additionally, numerical modeling has participated in the definition and optimization of treatment strategies (Gélat et al. 2014), as well as in the verification of treatment feasibility (Chavrier et al. 2000; N'Djin et al. 2015) and can provide an alternative to animal testing.

The simulation of HIFU treatment requires three models: ultrasound propagation, heat transfer, and thermal damage models. Several methods have already been described in the literature. For linear wave propagation computation, the Rayleigh integral method (Kirkup 1994) and the angular

spectrum method (Zeng and McGough 2008) are commonly used in homogeneous media and the hybrid angular spectrum method (Vyas and Christensen 2008) is chosen for computation in heterogeneous tissues. Heat transfer in biological tissues can be modeled by various models, including the non-Fourier bioheat transfer equation (Kundu and Dewanjee 2015), the microvascular-based model (Chen and Holmes 1980; Weinbaum et al. 1984) or the porous media theory (Mohammadpour and Firoozabadi 2020; Nakayama and Kuwahara 2008; Wessapan and Rattanadecho 2020; Yuan 2009). However, the most widely used is the Pennes BHTE (Pennes 1948), which is modeled with partial differential equations. This equation can be discretized with finite difference, finite element or finite volume methods (Tadmor 2012) on meshes of different types (Thompson et al. 1998). In some thermal models, changes in tissue acoustic properties during treatment can be considered (Garnier et al. 2008; Guntur and Choi 2020). Finally, thermal damage can be estimated with the Cumulative Equivalent Minutes at 43 °C (CEM43) value (Sapareto and Dewey 1984) or with the Arrhenius damage integral (Orgill et al. 1998). Open access tools already integrate some of these methods, such as the HITU simulator (Soneson 2015), Field II (Jensen and Svendsen 1992) or k-wave (Treeby et al. 2012).

These models are currently used to simulate HIFU treatment on abdominal organs (N'Djin et al. 2015; Schwenke et al. 2017), on the skull and brain (Padilla et al. 2018) or on other targets. However, these simulations only consider HIFU treatment effects on static organs. Only a few examples highlight the respiratory motion impact on HIFU treatment of abdominal organs, such as the liver (N'Djin et al. 2015; Schwenke et al. 2017; Zhang and Chauhan 2020). N'djin *et al.* (N'Djin et al. 2015) presented 3D numerical modeling of HIFU treatment in the liver using *in vivo* motion data obtained with the US-speckle tracking method and provides realistic results, as experimental data are used as inputs for simulations. However, this motion model only considers a 2D rigid motion because respiratory motion is mostly described in the cranial caudal direction. Schwenke *et al.* (Schwenke et al. 2017) presented a thermal model to simulate HIFU treatment in the liver using a Lagrangian approach to describe and resolve the heat transfer equation. Their work focuses on discontinuous motion considerations to study boundary sliding effects and computation time reduction to approach real-time simulation during clinical procedures. Nevertheless, precomputation of ultrasonic pressure fields, enabling real time computation, can also be responsible for long pretreatment work and reduction in result precision. Zhang *et al.* (Zhang and Chauhan 2020) presented a near real-time model based on

77 the fast explicit dynamics finite element method and considering soft tissue deformation. This model
78 provides accurate results for short computation times; but their study is only focused on liver cases.
79 Despite several studies in cardiac biomechanics and the emergence of cardiac modeling as a
80 diagnostic tool to understand physiopathological heart mechanisms (Humphrey 2002), the influence of
81 heart motion on HIFU treatment delivery is poorly documented. To our knowledge, there is no
82 simulation method of HIFU thermal ablation on a beating heart.

83 The purpose of this paper is to describe a numerical method to simulate the HIFU thermal
84 procedure in elastic and mobile heart models. This work is based on four simulation methods. Motion
85 and deformation of the heart muscle are evaluated by registration of 4D (3D+t) CT-scan images of a
86 heart cycle. Ultrasound propagation is modeled by the classical Rayleigh integral method. The thermal
87 model is built on the Pennes BHTE on static organs. However, to follow the temperature of each point
88 of the computation zone along the deformation cycle, the approach described in this paper consists of
89 solving the BHTE on a 3D nonorthogonally structured curvilinear grid using the finite volume method.
90 Finally, the thermal damage model is described with the CEM43 value.

91 The remainder of this paper is organized as follows: first, mathematical theory used to predict
92 HIFU thermal effects on moving and deformable tissues is developed; the application of the
93 implemented simulation method on a clinical case to compare thermal effects of HIFU treatment
94 depending on motion type and amplitude in two different regions of the heart is then described;
95 discussions are presented in the following section; and finally, conclusions of the study are provided.

96 **Simulation methods**

97 Simulation overview

98 Simulation of a thermal treatment with organ motions must encompass four aspects: motion
99 evaluation, acoustic propagation, heat transfers and thermal damage evaluation. Motion evaluation is
100 not the main subject of this article and is largely treated in the medical image registration literature
101 (Hoogendoorn et al. 2013). Common elastic registration techniques are used in the present work.
102 Acoustic propagation simulation is approached with linear equations. Therefore, most of the
103 challenges arising from tissue deformation are due to the influences of deformation on the heat
104 transfer equation discretization. The Bio Heat Transfer Equation (BHTE), commonly used in biological
105 tissue (Chato 1990; Pennes 1948), is derived from the general heat transfer equation as follows:

$$\rho_t c_t \frac{\partial T_P}{\partial t} = \boldsymbol{\nabla}. k_t \boldsymbol{\nabla} T_P + \omega_b c_b (T_A - T_P) + Q \quad (1)$$

where T_P (°C) is the temperature at point P and time t, ρ_t (kg.m^{-3}) is the tissue density, c_t (J.kg^{-1}.°C^{-1}) is the tissue specific heat, k_t (W.m^{-1}.°C^{-1}) is the tissue thermal conductivity, ω_b (kg.m^{-3}.s^{-1}) is the tissue blood perfusion rate, c_b (J.kg^{-1}.°C^{-1}) is the blood specific heat, T_A (°C) is the arterial blood temperature and Q (W.m^{-3}) is the source term, which here, is due to the energy added to the medium by ultrasound tissue absorption. To numerically solve Equation 1 within the scope of elastic and mobile organs, the challenge is to follow the motion of each point of the computation zone to evaluate throughout its displacements the heating (needed for temperature evaluation) and the exposure time (needed for thermal damage evaluation) at each time step.

Consequently, all the numerical solutions based on rigid grids cannot accurately describe thermal evolution in highly deformable muscle, as tissue contraction and dilatation continuously modify the anatomical geometry. To solve this problem, deformable grid fitting local deformation is used. Many teams have developed methods to solve similar partial derivative equations on mesh grids fitting complex geometrical models. This work is derived from finite volume methods described in the *Handbook of Numerical Heat Transfer* (Minkowycz et al. 2008) and S.E. Norris' thesis (Norris 2000).

Deformed model definition

The moving heart model is obtained from 4D CT-scans of a heart cycle (3D + t) divided into 20 time phases by the segmentation and nonrigid registration of the dataset. Tissue segmentation describes the anatomic structure of the numerical heart phantom, and image registration provides motion and deformation information between phases (refer to Appendix A).

To solve our partial derivative problem, the space is discretized into hexahedral cells. The initial phase of the heart cycle defines the reference grid that corresponds to a nondeformed frame. The other phases of the cycle define curvilinear grids that are generated from the displacement of the reference grid centroids to their new location and that correspond to deformed frames (Fig. 1).

Each grid is composed of hexahedral cells, with each cell described by its centroid $\mathcal{P}$, six faces t, b, n, s, w, e and eight vertices, which are the barycentric center of each neighboring cell centroid (Fig. 2). Because the reference grid spatial discretization can be different from the heart

phantom segmentation, displacement vectors are linearly interpolated in each centroid position. After deformation, the curvilinear grid is considered 3D, nonorthogonal, smooth and structured.

Ultrasonic field simulation

Ultrasonic fields obtained from any ultrasound propagation models can be used as input data for the thermal model. However, in this study, ultrasonic fields are computed using the Rayleigh integral equation (Arditi et al. 1981; Maynard and Williams 1982). A unique pressure simulation is computed for the first phase of the heartbeat on a 3D orthonormal grid. The medium is considered to be attenuating, homogeneous, and isotropic, while refraction and reflection are not considered in the field of computation. Ultrasonic propagation is evaluated in a voxel space. To calculate the attenuation, the shortest lines between two points of the finite medium are drawn for the whole computed zone. Under the hypothesis of constant speed in tissues, the attenuation along each line is then calculated by summing the attenuation of each tissue voxel crossed by the line. In the other phases of the heartbeat, the same pressure field is applied with the same acoustic parameters, but the centroid coordinates of each cell in the reference grid are remapped to the curvilinear coordinates from the corresponding displacement maps.

BHTE discretization on a curvilinear grid

The computation of heat transfer in biological tissues requires the application of the BHTE equation. As the equation is defined on a continuous space, we discretize it with the finite volume method.

First, BHTE is spatially integrated on a cell defined by its volume V as follows:

$$\underbrace{\iiint_V \rho_t c_t \frac{\partial T_P}{\partial t} dV}_{transient\ \Phi_T} = \underbrace{\iiint_V \boldsymbol{\nabla}.\, k_t \boldsymbol{\nabla} T_P dV}_{diffusion\ \Phi_D} + \underbrace{\iiint_V \omega_b c_b (T_A - T_P) dV}_{perfusion\ \Phi_{perf}} + \underbrace{\iiint_V Q dV}_{source\ \Phi_Q} \quad (2)$$

The rate of change of the tissue temperature can be attributed to three physical phenomena, which are accounted for by individual terms of the right-hand side of equation 2: diffusion, perfusion, and thermal energy deposition. Each term is discretized separately and temporally integrated as detailed in Appendix B.

The discretized solution of the equation is defined as follows:

$$T_P^{t+dt} = T_P^t + \frac{\Delta t}{\rho_t c_t}.\left(\frac{1}{V}\sum_{f=t,b,n,s,w,e} \Phi_{D_f}^t + \omega_b c_b (T_A - T_P^t) + Q\right) \quad (3)$$

where Φ_{D_f} is the diffusion through an elementary cell, and it is defined as the sum of the diffusion on each face of the cell. For the face ($\mathcal{E}$), the equation is written as follows:

$$\Phi_{D_e} = \underbrace{k_{t_e} G^1 (T_E - T_P)}_{orthogonal} + \underbrace{k_{t_e} G^2 (T_{ne} - T_{se}) + k_{t_e} G^3 (T_{te} - T_{be})}_{curvilinear} \quad (4)$$

where G^1, G^2 and G^3 are local geometry functions of the cell surface, which are defined with s^i being the surface vector and d_i being the distance vector as follows:

$$G^1 = \frac{\boldsymbol{s^1}.\boldsymbol{s^1}}{\boldsymbol{d_1}.\boldsymbol{s^1}};\ G^2 = \frac{\boldsymbol{s^2}.\boldsymbol{s^1}}{\boldsymbol{d_2}.\boldsymbol{s^2}};\ G^3 = \frac{\boldsymbol{s^3}.\boldsymbol{s^1}}{\boldsymbol{d_3}.\boldsymbol{s^3}} \quad (5)$$

The time step dt defined in Equation 3 must satisfy the Von Neumann criterion (Crank and Nicolson 1947).

Thermal dose

The Cumulative Equivalent Minutes at 43 °C (CEM43) described by Sapareto and Dewey (Sapareto and Dewey 1984) is an empirical value for estimating thermal damages induced by heating in tissues, which is given as follows:

$$t_{43°C}(t) = \int_0^t R^{43-T(t)}\, dt, \qquad R = \begin{cases} 0 & T < 37°C \\ 0.25 & T \in [37°C; 43°C] \\ 0.5 & T > 43°C \end{cases} \quad (6)$$

where $t_{43°C}$ is the equivalent time at 43 °C and T is the temperature at time t. According to the literature, the thermal dose threshold to create an irreversible lesion in soft tissues corresponds to a 240-min thermal exposure at 43 °C (Damianou and Hynynen 1993).

Numerical computation

To simulate thermal ablation in the moving heart, the numerical phantom heartbeat is divided into 20 phases, which are repeated in time in a cyclic motion. For each phase, motion and deformations are accounted for instantaneously in the computation as a snapshot, and no volume variation is considered between the phases. Thus, as previously hypothesized, cell volumes are assumed constant during the computed phase.

The numerical model resolution is computed according to the following pattern. First, to evaluate the ultrasonic field, the Rayleigh integral equation is computed point-by-point in the selected area, considering a discretized transducer ($\lambda/3$) as an emitting source. Deformations are then applied on each centroid of the reference grid, with the vertex of each cell being estimated as a barycenter of their surrounding centroids. Then, local geometry functions G^i (Equation B.10) are computed for each face of every cell and are saved. Thermal conductivity k is linearly interpolated at the cell faces. Volumes are evaluated according to Grandy *et al.* (Grandy 1997). According to the Von Neumann criterion, time step discretization is estimated from the smallest cell after deformation. The source term is interpolated from the ultrasonic field to the new deformed grid. Finally, Equations 3 and 6 are applied for each cell at every time step. Cell temperatures calculated to exceed 100 °C are forced to 100 °C for each time step, based on the hypothesis that vaporization occurs and temperature stays constant (Blauth et al. 2020). If a time step goes over a phase time length, the time step is reduced to the phase time length. Then, the next phase geometry and its corresponding properties are loaded for the next computation. The results are stored in a 3D cartesian grid where the locations of the curvilinear grid points are estimated using the stencil walk algorithm (Sadarjoen et al. 1998).

The numerical model is implemented in C++ on the CIVA platform (CEA-LIST). Computations are operated on a Dell Tower 7810 computer. The ultrasonic field and BHTE resolution are parallelized using Microsoft C++ AMP on the GPU (Nvidia GeForce GTX 1080) and the CPU (Intel, Xeon® E5-2620), respectively.

Simulation of a clinical case

Targeted zones

Two different areas of the numerical heart phantom are targeted: the atrioventricular node (AVN) and the ventricles apex (VA) (Fig. 3). The AVN is approximately the junction between the four cardiac cavities where the electrical impulse from the atria propagates in the ventricles. It represents atria motion and is treated with an esophageal approach. The VA, located at the bottom of the heart, is treated with a stomach approach. The targets are located at a distance of 55 mm for the AVN and 40 mm for the VA from the ultrasound probe. The motion amplitudes in the AVN and the VA regions are extracted from displacement maps computed for the deformed model (Appendix A) and are [dX, dY, dZ] = [9.89±5.12, 13.45±8.83, 6.94±4.89] and [3.92±4.2, 1.70±1.05, 5.38±3.99], with dX, dY and dZ

being the displacement amplitude in each dimension in millimeters. The tissue properties are detailed in Table 1. The model, as defined in the manuscript, considers the heat-sink effect through a mean perfusion coefficient, valid in any regions of the heart.

Ultrasound probe

HIFU is produced with a 3-cm² truncated spherical transducer operating at 3 MHz (Vermon, Tours, France). The transducer is composed of 8 rings, truncated at 14 mm. It has a 40-mm natural focal length, and it is able to focus electronically in a range of 17 to 55 mm from the transducer surface (Greillier et al. 2018) (Fig. 4). As the probe is designed to be used clinically with a transesophageal approach, its movements in the esophagus can be limited. This constraint should be considered numerically to fit in with real applications. Therefore, electronic steering is required to target any regions of the heart without moving the ultrasound source. This source is considered in the ultrasound propagation model with a $\lambda/3$ discretization.

Simulation parameters

On each targeted area, two types of simulations are conducted: one on a static heart to illustrate the results obtained with a static numerical model (Chavrier et al. 2000) and one on a mobile and deformable heart using the theory described in this paper (referred to in section *Simulation methods*). For each simulation, a single continuous sonication is performed at an acoustic power of 32 W, corresponding to an acoustic intensity of 10.6 W/cm² at the transducer surface. The dimensions of the -3 dB focal zone are 1.5625×12.5×0.625 mm³ for the AVN and 0.3125×1.25×6.875 mm³ for the VA. The heart rate is set to 60 beats per minute (1 Hz). The exposure duration is adapted to reach a lesion volume of 30 mm³.

Motion influence on the treatment efficacy and duration

The influence of motion on the treatment is evaluated with the following parameters: temperature distribution, $t_{43°C}$ distribution (CEM43), volumetric lesion similarity using the Dice-Sorensen coefficient (DSC) (Dice 1945; Sørensen 1948), undertreated lesion volume corresponding to the lesion volume appearing in the static heart but not in the moving heart (V_{under}), overtreated lesion volume corresponding to the lesion volume appearing in the moving heart and not in the static heart (V_{over}) and required duration reaching a 30-mm³ lesion volume (t_v).

Temperature maps are obtained with the new model and are represented in °C for values exceeding 43 °C. Thermal dose maps are calculated with Equation 6 from temperature maps. All the results are calculated in seconds and represented in $\log_{10}(t_{43°C})$ with $t_{43°C}$ in seconds.

The volume of the irreversible lesion is assessed in the thermal dose map, at the end of the simulation, in the nondeformed grid of the computation space. The number (N) of voxels in the computed area exceeding the CEM43 thermal dose threshold of 14000 seconds is counted, and the value is multiplied by the volume of one voxel, also called the elementary volume ($V_e = 0.3125^3$ mm^3) as follows:

$$V = N \times V_e \tag{7}$$

Volumetric differences in lesion formation are assessed by DSC. DSC considers the volumetric overlap between the two samples (lesion in the static heart or in the moving heart) to estimate the volumetric similarity between them as follows:

$$DSC[\%] = \frac{2 \times V_s \cap V_m}{V_s + V_m} \times 100 \tag{8}$$

where V_s and V_m are the lesions in the static heart and in the moving heart, respectively. However, the dissimilarity is studied by determining the undertreated (respectively overtreated) volume ratio due to motion as follows:

$$R_{u/o}[\%] = \frac{V_{u/o}}{V_s} \times 100 \tag{9}$$

where R_u and R_o are the undertreated and overtreated volume ratios, respectively, V_s is the reference volume (in the static heart), V_u is the undertreated lesion volume and V_o is the overtreated lesion volume.

To evaluate the time required to treat a specific volume of tissue, t_v, the treatment of the AVN region in the moving heart is used as a reference, as it is harder to obtain a large thermal lesion considering the motion amplitude in the AVN. From this simulation, the thermal lesion volume to reach is determined with the method described above. Then, with the other configuration, the thermal lesion volume is calculated at different steps by only considering the lesion at the focal zone and excluding

potential secondary lesions. The time step at which the lesion volume is closest to the reference volume is chosen.

All the results were postprocessed with MATLAB 2019b (The MathWorks Inc., Natick, MA, USA).

Results

Treatment duration

The required duration to treat the same volume of tissue differs depending on the treatment region. In a static configuration, reaching a (29.75±0.64)-mm^3 volume takes 4 s in the ventricular apex compared to 13 s in the atrioventricular node. Each region responds differently to motion. In the ventricular apex, treating the same volume with motion takes 3.6 s, corresponding to a 10% decrease compared to duration in static simulation. In the atrioventricular node, treatment duration increases substantially with motion. The duration is increased by a factor of 41 compared to the static configuration with a value of 9 min. All the results are gathered in Table 2.

Thermal lesion in the ventricular apex

The effects of motion on temperature maps, thermal dose distribution, and lesion spread are also important. The maximum temperature reached at the focus at the end of sonication is 100 °C in the static configuration and 73.42 °C in the moving configuration. As expected, the thermal spatial distribution is more diffused, and the values are lower with motion (Fig. 5). The variability in thermal dose distribution leads to variability in lesion spread and shape (Fig. 6), with a volumetric similarity of 40.82%. The undertreated and overtreated regions correspond to 55.67% and 57.22% of the reference lesion (in the static heart).

Thermal lesion in the atrioventricular node

Similar results are observed in the atrioventricular node. During the last phase, the maximum temperature reached in the focal zone is 82.29 °C in the static configuration and 51.75 °C in the moving configuration. The highest variability in temperature and lesion spread is observed between static and moving simulations in the atrioventricular node (Fig. 5), and the lesion shape is substantially different (Fig. 7). The volumetric similarity between simulations with or without motion is of 19.09%.

The dissimilarity is estimated using the undertreated and overtreated volume ratios, which are 81.26% and 77.67%, respectively.

Discussion

This paper introduces the theory of a thermal model to predict HIFU treatment effects on mobile and elastic organs. The novelty of the method is the consideration of organ motion and deformations within the heat transfer computation for cardiac applications. Moreover, the Eulerian method is used to offer a different resolution approach based on well-documented references (Minkowycz et al. 2008; Norris 2000). The BHTE is numerically resolved with the finite volume method on a 3D nonorthogonal and structured curvilinear grid. By considering heart deformations, the ultrasound pressure field, the temperature and the thermal dose are calculated at each time step and can be displayed in both computational and physical space thanks to the stencil walk algorithm.

This simulation method is applied to a specific clinical case: the treatment of focal cardiac arrhythmias with HIFU. The results provide information to study the influence of motion on treatment efficacy and accuracy, as well as on potential side effects. According to targeted region and motion consideration, considerable variability is observed when comparing treatment duration to reach the same lesion volume. Treatment in AVN takes more time than in VA. This difference could be explained by the treatment approach. The AVN is an internal structure located 55 mm from the transducer. In contrast, the VA is an external structure situated at a distance of 40 mm from the transducer. In the simulations, the anatomical configuration is simplified, and the esophagus (for AVN) and stomach (for VA) layers are not considered in the pressure field computation. Thus, ultrasound propagates through more structures and more distance to reach the AVN target than for VA. To treat VA, ultrasound only propagates through water, and thus, the beam is not attenuated, and lesion formation is faster. In AVN, ultrasound is highly attenuated by myocardium layers, increasing the treatment duration. Attenuation compensation could be considered to ensure the same intensity *in situ* in both locations, but the choice was made to apply the same power as the aim of the study was to understand the relative variation between simulated cases.

Treatment duration variability could also be explained by the influence of motion. In VA, motion speeds up lesion formation because static simulation only depends on diffusion to enlarge the lesion, while motion can contribute to lesion extension by focusing ultrasound on nearby points. These

variations explain the similar shape but different spread of the lesion. In AVN, motion substantially increases the treatment duration, and the lesion shape and the spread are considerably altered. As the motion amplitude is large, a temperature rise is produced in the targeted region, as well as in the surrounding tissue. In both cases, substantial variability in thermal dose distribution and spread is observed. This could lead to a decrease in treatment efficacy due to lesion size reduction in the targeted zone or result in the diminution of treatment accuracy due to secondary lesions in untargeted regions.

Although motion is mainly responsible for the extended treatment duration, perfusion effects also contribute. The temperature increase at the targeted point is considerably limited by the convective cooling effect of blood perfusion. In the model, the heat sink effect is only considered through the perfusion rate coefficient, which is the same for both targeted regions. However, from a medical point of view, the heart is composed of four cavities continuously filled by blood and is irrigated by small vessels. As described in the literature, creating HIFU lesions close to vessels is highly challenging because of blood flow (Cilleros et al. 2021; Mohammadpour and Firoozabadi 2020). The heat sink effect is even more critical in cardiac application, as blood circulates both in heart cavities and in vessels irrigating it (Wu et al. 2015). The AVN is located at the center of the four cardiac chambers, creating a lesion in this region could be more difficult than in the VA, which is located between two cavities at the heart tip. Considering perfusion effects due to blood flow in large chambers and in small coronary arteries differently in the model could be interesting to understand their consequences on AVN or VA ablations.

Some limitations may still be acknowledged in the model theory. Under the hypothesis that acoustic properties are not notably different between healthy tissue and ablated tissue, the ultrasound propagation map is only computed once on the first frame of the heartbeat cycle. The other frames are not recomputed, but motion is considered in the thermal model by remapping coordinates of each cell centroid in the reference grid to new curvilinear coordinates, from displacement maps. While this reduces computation time, this means that changes in tissue acoustic properties due to lesion formation are not considered for the computation of pressure field maps and consequently for temperature maps. Moreover, Guntur *et al.* (Guntur and Choi 2020) recently demonstrated that underestimating thermal parameter variation can cause a difference of 23% in the temperature

distribution. Studying the influence of thermal parameter variation in this manuscript could be interesting to fit the experimental results of the forthcoming validation study.

In the thermal model, arterial blood temperature is assumed to be constant. In some therapeutic applications, this temperature could increase during sonication and alter the treatment effects. However, as blood absorption is negligible, the arterial blood temperature increase is low, and the risk of lesions on vessels is reduced. In fact, our model mainly involves the arterial blood temperature in perfusion effects during HIFU treatment. As the blood flow is important near the heart, it can be assumed that the flow can maintain the arterial blood temperature constant enough to contribute to cooling effects during HIFU sonication.

Volume, and consequently density, is assumed constant in deformation evaluation during each computed phase, as a snapshot, and only varies instantly between two phases. This assumption follows historical guiding principles of similar papers hypothesizing that myocardium muscle is incompressible (Humphrey 2002); thus, variability between phases could be neglected. However, neglecting it may result in variability in the current results. Furthermore, all the simulations are computed with a spatial resolution of 0.3125 mm to fit the resolution of the deformation maps. A convergence study is carried out, as referred to in Appendix C, and demonstrates, in a specific case, that the thermal model converges for spatial resolutions lower than 0.4 mm. Even if the convergence study is not performed in the beating heart model, the simulation parameters are similar to the cardiac model and support the belief that the simulations presented in this manuscript can be considered accurate. However, a more specific convergence study using the beating heart model should still be conducted. In addition, heart simulation inputs are not as precise as real heart biomechanics. In this model, registration parameters do not consider the whole biomechanical complexity of heart motion, particularly torsion. The image registration quality is highly dependent on the raw data (quality, resolution, imaging modality, etc.) and the chosen parameters. Even if some methods of measuring heart torsion are well-established (Lehmonen et al. 2020), torsion evaluation is difficult and time-consuming. Further studies should be conducted to evaluate the impact of torsion variation on HIFU treatment efficiency and to determine if more precise deformation fields are required.

Finally, all simulations are computed with a fixed sonication power of 32 W. This value is chosen to adhere to the known limits of the HIFU probe, which will be used for future experimental

validation of the model. However, this high power could be the source of nonlinearity. Preliminary studies, based on Sapozhnikov's method to reconstruct an acoustic plane at the surface of the transducer from a measured plane (Sapozhnikov et al. 2003) and on Westervelt equations to estimate nonlinear effects (Lafond et al. 2017), demonstrate that nonlinearity is low at this sonication power. In any case, the model described in this paper is a thermal model and it can use any results from the ultrasound propagation model, in linear or nonlinear cases, to simulate temperature variation in ultrasound therapy.

Improvements can also be provided in the model application. Simulations are currently conducted with raw data from a single healthy heart. Other datasets could be considered to study motion effects considering specific heart anatomy, biomechanics, or electrophysiological responses. In this study, the secondary lesions close to the transducer are not considered, as the analysis is related to the influence of motion on the focal zone. However, to define treatment strategies, secondary lesions should be considered a potential adverse event. Consequently, cooling effects of the water balloon around the transducer should also be modeled as a means of reducing secondary lesions close to the transducer. As surrounding tissues are not included in these simulations, future work examining the influence of these layers on the heat deposition may be of interest.

Despite the stated limitations, the model provides very promising results. Simulations contribute to the understanding of heart mechanisms and motion consequences on CA treatments with HIFU. These results also contribute to an explanation of the low rate of successful thermal lesions during the last *in vivo* experiments (Greillier et al. 2018). This study confirms the necessity of adapting and optimizing CA treatment strategies according to motion and targeted regions. To ensure treatment efficacy and accuracy, the lesion should be restrained to the targeted zone. Two options could be considered: applying a duty cycle on sonication to treat only during diastole or using a tracking system to follow the targeted point during the whole treatment.

Further studies should be conducted on the model to provide numerical and experimental validation, which could examine the difference between simulated and experimental results, and thus, could further enhance the accuracy of the model.

Conclusion

In this paper, a novel numerical thermal model for HIFU ablation in mobile and elastic organs is presented. By discretizing and resolving the BHTE on a curvilinear grid, the model is able to simulate heat transfers in mobile and elastic organs. Simulations are computed for a clinical case of cardiac arrhythmia treatment and provide realistic results. The study demonstrates that targeted regions and motion considerably influence treatment duration, lesion shape, and spread. It also emphasizes the importance of considering motion in HIFU treatment simulation to define efficient and accurate treatment strategies. Further studies will validate the model experimentally and investigate HIFU treatment strategies for cardiac arrhythmia therapy.

Acknowledgements: This work was supported by the French National Research Agency (ANR) under the CHORUS Grant project ANR17-CE19-0017 and the SATURN Grant project ANR15-CE19-0016. The author would like to thank Dr. R. Andrew Drainville for proofreading the manuscript.

Conflict of Interest Statement: The authors declare that they have no conflicts of interest.

Appendices

Appendix A. Numerical phantom

Our simulation uses a numerical phantom obtained from 4D medical images of a heart cycle (3D + t). This cycle is divided into 20 time phases acquired by a contrast CT-scan with a spatial resolution of 0.3125^3 mm^3. From these images, tissues are segmented, and motions and deformations are obtained by image registration (Fig. A.1).

Tissue segmentation, motion and deformation of these tissues are estimated using the methods described by Sandoval *et al.* (Sandoval 2015). Image segmentation consists of dividing medical images into finite tissue regions. First, the first frame tissues are segmented semiautomatically in ITKSnap using Active Contours. Then, an affine and elastic registration (Bspline deformation model and Mutual Information as similarity measure) is performed between each consecutive gray level volume of the sequence using the Elastix Library (Klein et al. 2010). The registration estimates the tissue deformation as the displacement of each voxel from the first phase to their new position at each phase. Therefore, for any voxel with a center M(x,y,z,t_0) at the first phase, its new location M'(x',y',z',t_n) after deformation at a given phase n is as follows:

$$\boldsymbol{OM}'(x',y',z',t_n) = \boldsymbol{OM}(x,y,z,t_0) + \boldsymbol{v_n}(x,y,z) \tag{A.1}$$

where O is the reference point and $\boldsymbol{v}_n$ is the displacement vector corresponding to the phase n.

These consecutive registrations are used to propagate the tissue segmentation to the other frames and to estimate the displacement of the tissue voxels among the sequence.

Appendix B. BHTE discretization: Mathematical theory

This section details the BHTE discretization over a curvilinear grid. Heat transfer computation in biological tissues implies the BHTE resolution. As the equation is defined on a continuous space, we discretize it with the finite volume method.

First, BHTE is spatially integrated on a cell defined by its volume V as follows:

$$\underbrace{\iiint_V \rho_t c_t \frac{\partial T_P}{\partial t} dV}_{transient\ \Phi_T} = \underbrace{\iiint_V \boldsymbol{\nabla}.\, k_t \boldsymbol{\nabla} T_P dV}_{diffusion\ \Phi_D} + \underbrace{\iiint_V \omega_b c_b (T_A - T_P) dV}_{perfusion\ \Phi_{perf}} + \underbrace{\iiint_V Q dV}_{source\ \Phi_Q} \tag{B.1}$$

The equation is composed of 4 terms: diffusion, perfusion, source and transient. Each term is discretized separately.

Diffusion term (Φ_D) – This term describes spatial transfer between one tissue location and neighboring ones. The main issue to discretize it is the Laplacian. By defining an arbitrary closed surface, i.e., the cell surface, Φ_D is simplified by the divergence theorem and then discretized into each face of the cell as follows:

$$\Phi_D = \iiint_V \nabla . k_t \nabla T_P dV = \oiint_S k_t \nabla T_P \boldsymbol{dS} = \sum_{f=t,b,n,s,w,e} k_{t_f} \nabla T_P . \boldsymbol{S_f} \tag{B.2}$$

where t, b, n, s, w, e are the 6 faces of the cells, k_{t_f} is the linear interpolation of k_t with surrounding cells and $\boldsymbol{S} = S.\boldsymbol{n}$ is the surface vector, where $\boldsymbol{n}$ is the normal vector to the surface S.

The solution is developed only for face ($\mathcal{E}$), and the same method is applied for the other faces. By the chain rule, if composed of derivative functions, the gradient ∇T_P can be written as follows:

$$\nabla T_P = grad\ T_P = \frac{\partial T_P}{\partial x^j}\boldsymbol{u_j} = \frac{\partial T_P}{\partial \xi^m}.\frac{\partial \xi^m}{\partial x^j}\boldsymbol{u_j} \tag{B.3}$$

where $\boldsymbol{u^j}$ is the Cartesian system basis, $\boldsymbol{x^j}$ are the coordinates in the Cartesian coordinate system, and ξ^m are the coordinates in a new curvilinear covariant coordinate system. The geometrical relationship between the Cartesian system, curvilinear system, and its covariant and contravariant vectors are presented in Fig. B.1. By definition, contravariant vectors of the system are written as $\boldsymbol{e^m} = \frac{\partial \xi^m}{\partial x^j}\boldsymbol{u_j}$ in Einstein notation. Therefore, the gradient can be expressed as follows:

$$\nabla T_P = \frac{\partial T_P}{\partial \xi^m}.\boldsymbol{e^m} \tag{B.4}$$

Contravariant vectors can be expressed with covariant vectors as follows:

$$\mathbf{e^i} = \frac{\mathbf{e_j} \times \mathbf{e_k}}{\mathbf{e_i}.(\mathbf{e_j} \times \mathbf{e_k})} \tag{B.5}$$

where $\cdot$ is the scalar product, $\times$ is the vector product and (i, j, k) is the circular permutation of the reference frame. The contravariant vectors can be simplified as follows:

$$\boldsymbol{e^i} = \frac{\boldsymbol{e_j} \times \boldsymbol{e_k}}{\boldsymbol{e_i}.(\boldsymbol{e_j} \times \boldsymbol{e_k})}\frac{\delta\xi^j\delta\xi^k}{\delta\xi^j\delta\xi^k} = \frac{\delta\xi^j\boldsymbol{e_j} \times \delta\xi^k\boldsymbol{e_k}}{\boldsymbol{e_i}.(\delta\xi^j\boldsymbol{e_j} \times \delta\xi^k\boldsymbol{e_k})} = \frac{\mathbf{s^i}}{\mathbf{e_i}.\mathbf{s^i}} \tag{B.6}$$

where $\boldsymbol{s^i} = \delta\xi^j \boldsymbol{e_j} \times \delta\xi^k \boldsymbol{e_k}$ is called the surface vector, $\boldsymbol{sene} = \delta\xi^j \boldsymbol{e_j} = \boldsymbol{d_j}$ is the vector going from se to ne points and $\boldsymbol{bete} = \delta\xi^k \boldsymbol{e_k} = \boldsymbol{d_k}$ is the vector from be to te (Fig. 2). Considering the circular permutation, the other surface vectors are defined as $\boldsymbol{s^j} = \delta\xi^k \boldsymbol{e_k} \times \delta\xi^i \boldsymbol{e_i}$ and $\boldsymbol{s^k} = \delta\xi^i \boldsymbol{e_i} \times \delta\xi^j \boldsymbol{e_j}$ where $\boldsymbol{PE} = \delta\xi^i \boldsymbol{e_i} = \boldsymbol{d_i}$.

Thus, the flow over the (e) face of Equation B.3 can be approximated as follows:

$$\begin{aligned}\Phi_{P_e} &= \oiint_{S_e} \left(k_{t_e} \frac{\partial T_P}{\partial \xi^1} \boldsymbol{e^1} + k_{t_e} \frac{\partial T_P}{\partial \xi^2} \boldsymbol{e^2} + k_{t_e} \frac{\partial T_P}{\partial \xi^3} \boldsymbol{e^3} \right) \boldsymbol{dS_e} \\ &\approx k_{t_e} \frac{\partial T_P}{\partial \xi^1} . \mathrm{S}_e . \mathbf{n} \frac{\boldsymbol{s^1}}{\mathbf{e_1} . \mathbf{s^1}} + k_{t_e} \frac{\partial T_P}{\partial \xi^2} . \mathrm{S}_e . \mathbf{n} \frac{\boldsymbol{s^2}}{\mathbf{e_1} . \mathbf{s^2}} + k_{t_e} \frac{\partial T_P}{\partial \xi^3} . \mathrm{S}_e . \mathbf{n} \frac{\boldsymbol{s^3}}{\mathbf{e_1} . \mathbf{s^3}}\end{aligned} \tag{B.7}$$

As $\boldsymbol{S_e} = S_e . \boldsymbol{n}$ is the normal vector to a surface and is defined as the normal vector to the (e) face. The equation can be simplified as follows:

$$\begin{aligned}\Phi_{D_e} &\approx k_{t_e} \frac{T_E - T_P}{\delta\xi^1} \frac{\boldsymbol{s^1}}{\boldsymbol{e_1 s^1}} . \boldsymbol{s^1} + k_{t_e} \frac{T_{ne} - T_{se}}{\delta\xi^2} \frac{\boldsymbol{s^2}}{\boldsymbol{e_1 s^2}} . \boldsymbol{s^1} + k_{t_e} \frac{T_{te} - T_{be}}{\delta\xi^1} \frac{\boldsymbol{s^3}}{\boldsymbol{e_3 s^3}} . \boldsymbol{s^1} \\ &\approx k_{t_e} (T_E - T_P) \frac{\boldsymbol{s^1} . \boldsymbol{s^1}}{\boldsymbol{d_1} . \boldsymbol{s^1}} + k_{t_e} (T_{ne} - T_{se}) \frac{\boldsymbol{s^2} . \boldsymbol{s^1}}{\boldsymbol{d_2} . \boldsymbol{s^2}} + k_{t_e} (T_{te} - T_{be}) \frac{\boldsymbol{s^3} . \boldsymbol{s^1}}{\boldsymbol{d_3} . \boldsymbol{s^3}}\end{aligned} \tag{B.8}$$

For readability concerns, the equation is written as follows:

$$\Phi_{D_e} = \underbrace{k_{t_e} G^1 (T_E - T_P)}_{orthogonal} + \underbrace{k_{t_e} G^2 (T_{ne} - T_{se}) + k_{t_e} G^3 (T_{te} - T_{be})}_{curvilinear} \tag{B.9}$$

where G^1, G^2 and G^3 are local geometry functions of the cell surface:

$$G^1 = \frac{\boldsymbol{s^1} . \boldsymbol{s^1}}{\boldsymbol{d_1} . \boldsymbol{s^1}}; \; G^2 = \frac{\boldsymbol{s^2} . \boldsymbol{s^1}}{\boldsymbol{d_2} . \boldsymbol{s^2}}; \; G^3 = \frac{\boldsymbol{s^3} . \boldsymbol{s^1}}{\boldsymbol{d_3} . \boldsymbol{s^3}} \tag{B.10}$$

Each term illustrates the energy flow through the projection of S_e along each curvilinear basis component. The first term of the equation accounts for orthogonal energy flow, and the second and third terms are corrective terms for curvilinear geometry. Further explanation can be found in Norris' thesis (Norris 2000).

The diffusion Φ_f through an elementary cell is the sum of diffusion on each face. Under the hypothesis of constant geometry and time linearity during one phase, the diffusion term is temporally integrated as follows:

$$E_D \approx \int_t^{t+dt} \sum_{f=t,b,n,s,w,e} \Phi_{D_f}\, dt \approx \left[\sum_{f=t,b,n,s,w,e} \Phi_{D_f} \right]_t^{t+dt} \tag{B.11}$$

$$E_D \approx \left(\sum_{f=t,b,n,s,w,e} h\Phi_{D_f}^{t+dt} - (1-h)\Phi_{D_f}^{t} \right) \Delta t \tag{B.12}$$

where $h \in [0,1]$ is the time level weighting-factor and its value determines the equation form for different resolution schemes (Minkowycz et al. 2008).

Transient term (Φ_T) – The transient term describes the time effect in the equation as follows:

$$E_T = \int_t^{t+dt} \iiint_V \rho_t\, c_t \frac{\partial T_P}{\partial t}\, dV dt \tag{B.13}$$

Under the hypothesis of constant volume during time, the transient term is integrated as follows:

$$E_T = \rho_t c_t (T_P^{t+dt} - T_P^t) V \tag{B.14}$$

Perfusion term (Φ_{perf}) – The perfusion term, also named the heat sink, accounts for blood perfusion effects in tissues. Under the hypothesis of constant volume and time linearity, the perfusion term is integrated as follows:

$$E_{perf} = \int_t^{t+dt} \iiint_V \omega_b\, c_b (T_A - T_P) dV dt \tag{B.15}$$

$$E_{perf} = \omega_b c_b [T_A - (hT_P^{t+dt} - (1-h)T_P^t)] \mathrm{V} \Delta t \tag{B.16}$$

Heat source (Φ_Q) – The heat source is the ultrasonic energy absorbed by the tissue. It was defined by Damianou *et al.* (Damianou and Hynynen 1993) as follows:

$$Q = F_{mu}.\alpha.f.\frac{p^2}{\rho.c} \tag{B.17}$$

where F_{mu} is the absorption ratio, α (Np.m^{-1}) is the acoustic attenuation, p (Pa) is the acoustic pressure, ρ (kg.m^{-3}) is the density, f (Hz) is the frequency and c (m.s^{-1}) is the speed of sound. Under the hypothesis of constant volume and time linearity, the source term is integrated as follows:

$$E_Q = \int_t^{t+dt} \iiint_V Q\, dV dt = QV\Delta t \tag{B.18}$$

where Q is calculated from pressure fields obtained previously. The pressure is computed in a different simulation grid, and its value is estimated by trilinear interpolation at the cell centroid.

Equation solution – Gathering all the equation terms, the equation is as follows:

$$\rho_t c_t (T_P^{t+dt} - T_P^t) V = \sum_{f=t,b,n,s,w,e} \left(h\Phi_{D_f}^{t+dt} - (1-h)\Phi_{D_f}^t \right) \Delta t + \omega_b c_b V [T_A - (hT_P^{t+dt} - (1-h)T_P^t)] \Delta t + QV\Delta t \quad \text{(B.19)}$$

By factorizing, the equation is as follows:

$$T_P^{t+dt} = T_P^t + \frac{\Delta t}{\rho_t c_t} \left(\sum_{f=t,b,n,s,w,e} \frac{h\Phi_{D_f}^{t+dt} - (1-h)\Phi_{D_f}^t}{V} + \omega_b c_b \left[T_A - \left(hT_P^{t+dt} - (1-h)T_P^t \right) \right] + Q \right) \quad \text{(B.20)}$$

In computational fluid dynamics (CFD), $h \in [0,1]$ gives information on the resolution type. Here, the explicit solution scheme ($h = 0$) is chosen for implementation concerns. The partial derivative equation must be solved with an adapted time step defined with the Von Neumann criterion (Crank and Nicolson 1947).

$$T_P^{t+dt} = T_P^t + \frac{\Delta t}{\rho_t c_t} . \left(\frac{1}{V} \sum_{f=t,b,n,s,w,e} \Phi_{D_f}^t + \omega_b c_b (T_A - T_P^t) + Q \right) \quad \text{(B.21)}$$

Appendix C. Model accuracy: the convergence study

In this section, the accuracy of the model is evaluated. Convergence of the results is assessed by studying quantitative result variation depending on the simulation spatial resolution.

As the beating heart model is complex, the study is carried out on a simplest model presenting the same properties as the heart. The model is a heterogeneous matrix (40×40×70mm^3) composed of two tissues (myocardium and blood) with the properties described in Table 1, and undergoing helical displacements, with an absolute amplitude of [dX, dY] = [3.11, 17.16] mm. Periodic motion repetition is set to 1 Hz.

The simulated ultrasound probe is the same as that described in section 3.2. Sonication is performed continuously at an acoustic power of 32 W (acoustic intensity of 10.6 W/cm^2) at the transducer surface for 5 s, with a 36-mm focus. Simulations are computed with different spatial resolutions, ranging from

0.2 to 2 mm. For each simulation, the maximum temperature in the focal zone is selected and compared to the reference. The reference temperature is the value obtained with the smallest spatial resolution. To consider the convergence of the model, the temperature values should be consecutively included in the 5%-interval around the reference temperature.

The convergence interval is [64.99, 68.33] °C in position 1 and [57.95, 60.93] °C in position 2. The model starts to converge for a number of elements higher than 7.1×10^5, corresponding to a spatial resolution of 0.4 mm (Fig. C.1 and Table C.1).

The results may still be subject to small variation, since the Von Neumann criterion is used to ensure model stability, which links the time step with the spatial step. As the spatial step varies in our convergence study, the time step also changes and the final temperature results can fluctuate.

References

Arditi M, Foster FS, Hunt JW. Transient fields of concave annular arrays. Ultrason Imaging 1981;3.

Bawiec CR, N'Djin WA, Bouchoux G, Sénégond N, Guillen N, Chapelon JY. Preliminary Investigation of a 64-element Capacitive Micromachined Ultrasound Transducer (CMUT) Annular Array Designed for High Intensity Focused Ultrasound (HIFU). IRBM 2018;39:295–306.

Bessiere F, N'djin WA, Colas EC, Chavrier F, Greillier P, Chapelon JY, Chevalier P, Lafon C. Ultrasound-guided transesophageal High-Intensity Focused Ultrasound cardiac ablation in a beating heart: a pilot feasibility study in pigs. Ultrasound Med Biol 2016;42:1848–1861.

Blauth S, Hübner F, Leithäuser C, Siedow N, Vogl TJ. Mathematical modeling of vaporization during laser-induced thermotherapy in liver tissue. JMathIndustry 2020;10:16.

Charrel T, Aptel F, Birer A, Chavrier F, Romano F, Chapelon JY, Denis P, Lafon C. Development of a Miniaturized HIFU Device for Glaucoma Treatment With Conformal Coagulation of the Ciliary Bodies. Ultrasound Med Biol 2011;37:742–754.

Chato JC. Fundamentals of Bioheat Transfer. In: Gautherie M, ed. Thermal Dosimetry and Treatment Planning Berlin, Heidelberg: Springer, 1990. pp. 1–56.

Chavrier F, Chapelon JY, Gelet A, Cathignol D. Modeling of high-intensity focused ultrasound-induced lesions in the presence of cavitation bubbles. Citation: The Journal of the Acoustical Society of America 2000;108:432.

Chen MM, Holmes KR. Microvascular Contributions in Tissue Heat Transfer. Ann N Y Acad Sci 1980;335:137–150.

Cilleros C, Dupré A, Vincenot J, Melodelima D. Development of a Simple In Vitro Artery Model and an Evaluation of the Impact of Pulsed Flow on High-Intensity Focused Ultrasound Ablation. IRBM 2021;42:112–119.

Constanciel E, N'Djin WA, Bessière F, Chavrier F, Grinberg D, Vignot A, Chevalier P, Chapelon JY, Lafon C. Design and evaluation of a transesophageal HIFU probe for ultrasound-guided cardiac ablation: Simulation of a HIFU mini-maze procedure and preliminary ex vivo trials. IEEE Trans Ultrason Ferroelectr Freq Control 2013;60:1868–1883.

Crank J, Nicolson P. A practical method for numerical evaluation of solutions of partial differential equations of the heat-conduction type. Mathematical Proceedings of the Cambridge Philosophical Society 1947;43:50–67.

Curiel L, Chavrier F, Souchon R, Birer A, Chapelon JY. 1.5-D high intensity focused ultrasound array for non-invasive prostate cancer surgery. IEEE Trans Ultrason Ferroelectr Freq Control 2002;49:231–242.

Damianou C, Hynynen K. The effect of various physical parameters on the size and shape of necrosed tissue volume during ultrasound surgery. J Acoust Soc Am 1993;95:1641–1649.

Dice LR. Measures of the Amount of Ecologic Association Between Species. Ecol Appl 1945;26:297–302.

Garnier C, Lafon C, Dillenseger JL. 3-D modeling of the thermal coagulation necrosis induced by an interstitial ultrasonic transducer. IEEE Trans Biomed Eng 2008;55:833–837.

Gélat P, ter Haar G, Saffari N. A comparison of methods for focusing the field of a HIFU array transducer through human ribs. Phys Med Biol 2014;59:3139–3171.

549 Gelet A, Chapelon JY, Bouvier R, Rouviere O, Lasne Y, Lyonnet D, Dubernard JM. Transrectal high-
550 intensity focused ultrasound: Minimally invasive therapy of localized prostate cancer. J
551 Endourol 2000;14:519–528.

552 Grandy J. Efficient Computation of Volume of Hexahedral Cells. Livermore, CA, 1997 Oct.

553 Greillier P, Ankou B, Bour P, Zorgani A, Abell E, Lacoste R, Bessière F, Pernot M, Catheline S,
554 Quesson B, Chevalier P, Lafon C. Myocardial Thermal Ablation with a Transesophageal High-
555 Intensity Focused Ultrasound Probe: Experiments on Beating Heart Models. Ultrasound in
556 Medicine and Biology 2018;

557 Guntur SR, Choi MJ. Temperature Dependence of Tissue Thermal Parameters Should Be Considered
558 in the Thermal Lesion Prediction in High-Intensity Focused Ultrasound Surgery. Ultrasound
559 Med Biol 2020;46:1001–1014.

560 Harris P, Lysitsas D. Ventricular arrhythmias and sudden cardiac death. BJA Education 2016;16:221–
561 229.

562 Hasgall P, Di Gennaro F, Baumgartner C, Neufeld E, Lloyd B, Gosselin M, Payne D, Klingenböck A,
563 Kuster N. IT'IS Database for thermal and electromagnetic parameters of biological tissues.
564 2018.

565 Hoogendoorn C, Duchateau N, Sánchez-Quintana D, Whitmarsh T, Sukno FM, De Craene M, Lekadir
566 K, Frangi AF, Hoogendoorn C, Lekadir K. A high-resolution atlas and statistical model of the
567 human heart from multislice CT. IEEE Trans Biomed Eng 2013;32:28–44.

568 Humphrey JD. Cardiovascular Solid Mechanics. Cardiovascular Solid Mechanics. Springer New York,
569 2002.

570 Jensen JφA, Svendsen NB. Calculation of Pressure Fields from Arbitrarily Shaped, Apodized, and
571 Excited Ultrasound Transducers. IEEE Trans Ultrason Ferroelectr Freq Control 1992;39:262–
572 267.

573 Ji Y, Hu K, Zhang Y, Gu L, Zhu J, Zhu L, Zhu Y, Zhao H. High-intensity focused ultrasound (HIFU)
574 treatment for uterine fibroids: a meta-analysis. Arch Gynecol Obstet 2017;296:1181–1188.

575 Kirkup SM. Computational solution of the acoustic field surrounding a baffled panel by the Rayleigh
576 integral method. Appl Math Model 1994;18:403–407.

577 Klein S, Staring M, Murphy K, Viergever MA, Pluim JPW. Elastix: A toolbox for intensity-based medical
578 image registration. IEEE Trans Biomed Eng 2010;29:196–205.

579 Kundu B, Dewanjee D. A new method for non-Fourier thermal response in a single layer skin tissue.
580 Case Stud Therm Eng 2015;5:79–88.

581 Lafond M, Prieur F, Chavrier F, Mestas J-L, Lafon C. Numerical study of a confocal ultrasonic setup
582 for cavitation creation. J Acoust Soc Am 2017;141:1953–1961.

583 Lehmonen L, Jalanko M, Tarkiainen M, Kaasalainen T, Kuusisto J, Lauerma K, Savolainen S. Rotation
584 and torsion of the left ventricle with cardiovascular magnetic resonance tagging: comparison
585 of two analysis methods. BMC Med Imaging 2020;1–8.

586 Maynard JD, Williams EG. Numerical evaluation of the rayleigh integral for planar radiators using the
587 fft. J Acoust Soc Am 1982;72:2020–2030.

588 Minkowycz WJ, Sparrow EM, Murthy JY, Abraham JP. Handbook of numerical heat transfer. John
589 Wiley and Sons. Hoboken, NJ, USA, 2008.

590 Mohammadpour M, Firoozabadi B. High intensity focused ultrasound (HIFU) ablation of porous liver:
591 Numerical analysis of heat transfer and hemodynamics. Appl Therm Eng 2020;170:115014.

592 Nakayama A, Kuwahara F. A general bioheat transfer model based on the theory of porous media. Int
593 J Heat Mass Transfer 2008;51:3190–3199.

594 N'Djin WA, Chapelon J-Y, Melodelima D. An Ultrasound Image-Based Dynamic Fusion Modeling
595 Method for Predicting the Quantitative Impact of In Vivo Liver Motion on Intraoperative HIFU
596 Therapies: Investigations in a Porcine Model. PloS one Public Library of Science,
597 2015;10:e0137317.

598 Norris SE. A Parallel Navier Stokes Solver for Natural Convection and Free Surface Flow [PhD thesis].
599 The University of Sydney, 2000. Available from: 10.13140/RG.2.1.5072.4964

600 Orgill DP, Solari MG, Barlow MS, O'Connor NE. A finite-element model predicts thermal damage in
601 cutaneous contact burns. J Burn Care Res 1998;19:203–209.

602 Padilla F, Loyet R, Moore D, Ouaked A, Snell J, Eames M, Chatillon S, Lafon C. Simulation of
603 ultrasound propagation through human skull: Experimental validation and application to
604 treatment planning. J Acoust Soc Am 2018;144:1748–1748.

605 Park Y, Jung NY, Na YC, Chang JW. Four-year follow-up results of magnetic resonance-guided
606 focused ultrasound thalamotomy for essential tremor. Mov Disord 2019;34:727–734.

607 Pennes HH. Analysis of tissue and arterial blood temperatures in the resting human forearm. Journal
608 of applied physiology 1948;1:93–122.

609 Pichardo S, Hynynen K. New design for an endoesophageal sector- based array for the treatment of
610 atrial fibrillation: A parametric simulation study. IEEE Trans Ultrason Ferroelectr Freq Control
611 2009;56:600–612.

612 Roth GA, Abate D, Abate KH, Abay SM, Abbafati C, Abbasi N, Abbastabar H, Abd-Allah F, Abdela J,
613 Abdelalim A, Abdollahpour I, Abdulkader RS, Abebe HT, Abebe M, Abebe Z, Abejie AN,
614 Abera SF, Abil OZ, Abraha HN, Abrham AR, Abu-Raddad LJ, Accrombessi MMK, Acharya D,
615 Adamu AA, Adebayo OM, Adedoyin RA, Adekanmbi V, Adetokunboh OO, Adhena BM, Adib
616 MG, Admasie A, Afshin A, Agarwal G, Agesa KM, Agrawal A, Agrawal S, Ahmadi A, Ahmadi
617 M, Ahmed MB, Ahmed S, Aichour AN, Aichour I, Aichour MTE, Akbari ME, Akinyemi RO,
618 Akseer N, Al-Aly Z, Al-Eyadhy A, Al-Raddadi RM, Alahdab F, Alam K, Alam T, Alebel A, Alene
619 KA, Alijanzadeh M, Alizadeh-Navaei R, Aljunid SM, Alkerwi A, Alla F, Allebeck P, Alonso J,
620 Altirkawi K, Alvis-Guzman N, Amare AT, Aminde LN, Amini E, Ammar W, Amoako YA, Anber
621 NH, Andrei CL, Androudi S, Animut MD, Anjomshoa M, Ansari H, Ansha MG, Antonio CAT,
622 Anwari P, Aremu O, Arnlov J, Arora A, Arora M, Artaman A, Aryal KK, Asayesh H, Asfaw ET,
623 Ataro Z, Atique S, Atre SR, Ausloos M, Avokpaho EFGA, Awasthi A, Ayala Quintanilla BP,
624 Ayele Y, Ayer R, Azzopardi PS, Babazadeh A, Bacha U, Badali H, Badawi A, Bali AG,
625 Ballesteros KE, Banach M, Banerjee K, Bannick MS, Banoub JAM, Barboza MA, Barker-Collo
626 SL, Barnighausen TW, Barquera S, Barrero LH, Bassat Q, Basu S, Baune BT, Baynes HW,
627 Bazargan-Hejazi S, Bedi N, Beghi E, Behzadifar M, Behzadifar M, Bejot Y, Bekele BB,
628 Belachew AB, Belay E, Belay YA, Bell ML, Bello AK, Bennett DA, Bensenor IM, Berman AE,
629 Bernabe E, Bernstein RS, Bertolacci GJ, Beuran M, Beyranvand T, Bhalla A, Bhattarai S,
630 Bhaumik S, Bhutta ZA, Biadgo B, Biehl MH, Bijani A, Bikbov B, Bilano V, Bililign N, Bin
631 Sayeed MS, Bisanzio D, Biswas T, Blacker BF, Basara BB, Borschmann R, Bosetti C,
632 Bozorgmehr K, Brady OJ, Brant LC, Brayne C, Brazinova A, Breitborde NJK, Brenner H,
633 Briant PS, Britton G, Brugha T, Busse R, Butt ZA, Callender CSKH, Campos-Nonato IR,
634 Campuzano Rincon JC, Cano J, Car M, Cardenas R, Carreras G, Carrero JJ, Carter A,
635 Carvalho F, Castaneda-Orjuela CA, Castillo Rivas J, Castle CD, Castro C, Castro F, Catala-
636 Lopez F, Cerin E, Chaiah Y, Chang JC, Charlson FJ, Chaturvedi P, Chiang PPC, Chimed-
637 Ochir O, Chisumpa VH, Chitheer A, Chowdhury R, Christensen H, Christopher DJ, Chung SC,
638 Cicuttini FM, Ciobanu LG, Cirillo M, Cohen AJ, Cooper LT, Cortesi PA, Cortinovis M, Cousin
639 E, Cowie BC, Criqui MH, Cromwell EA, Crowe CS, Crump JA, Cunningham M, Daba AK, Dadi
640 AF, Dandona L, Dandona R, Dang AK, Dargan PI, Daryani A, Das SK, Gupta DR, Neves DJ,
641 Dasa TT, Dash AP, Davis AC, Davis Weaver N, Davitoiu DV, Davletov K, De La Hoz FP, De
642 Neve JW, Degefa MG, Degenhardt L, Degfie TT, Deiparine S, Demoz GT, Demtsu BB,
643 Denova-Gutierrez E, Deribe K, Dervenis N, Des Jarlais DC, Dessie GA, Dey S, Dharmaratne

SD, Dicker D, Dinberu MT, Ding EL, Dirac MA, Djalalinia S, Dokova K, Doku DT, Donnelly CA, Dorsey ER, Doshi PP, Douwes-Schultz D, Doyle KE, Driscoll TR, Dubey M, Dubljanin E, Duken EE, Duncan BB, Duraes AR, Ebrahimi H, Ebrahimpour S, Edessa D, Edvardsson D, Eggen AE, El Bcheraoui C, El Sayed Zaki M, El-Khatib Z, Elkout H, Ellingsen CL, Endres M, Endries AY, Er B, Erskine HE, Eshrati B, Eskandarieh S, Esmaeili R, Esteghamati A, Fakhar M, Fakhim H, Faramarzi M, Fareed M, Farhadi F, Farinha CSE, Faro A, Farvid MS, Farzadfar F, Farzaei MH, Feigin VL, Feigl AB, Fentahun N, Fereshtehnejad SM, Fernandes E, Fernandes JC, Ferrari AJ, Feyissa GT, Filip I, Finegold S, Fischer F, Fitzmaurice C, Foigt NA, Foreman KJ, Fornari C, Frank TD, Fukumoto T, Fuller JE, Fullman N, Furst T, Furtado JM, Futran ND, Gallus S, Garcia-Basteiro AL, Garcia-Gordillo MA, Gardner WM, Gebre AK, Gebrehiwot TT, Gebremedhin AT, Gebremichael B, Gebremichael TG, Gelano TF, Geleijnse JM, Genova-Maleras R, Geramo YCD, Gething PW, Gezae KE, Ghadami MR, Ghadimi R, Ghasemi Falavarjani K, Ghasemi-Kasman M, Ghimire M, Gibney KB, Gill PS, Gill TK, Gillum RF, Ginawi IA, Giroud M, Giussani G, Goenka S, Goldberg EM, Goli S, Gomez-Dantes H, Gona PN, Gopalani SV, Gorman TM, Goto A, Goulart AC, Gnedovskaya VE, Grada A, Grosso G, Gugnani HC, Guimaraes ALS, Guo Y, Gupta PC, Gupta R, Gupta R, Gupta T, Gutierrez RA, Gyawali B, Haagsma JA, Hafezi-Nejad N, Hagos TB, Hailegiyorgis TT, Hailu GB, Haj-Mirzaian A, Haj-Mirzaian A, Hamadeh RR, Hamidi S, Handal AJ, Hankey GJ, Harb HL, Harikrishnan S, Haro JM, Hasan M, Hassankhani H, Hassen HY, Havmoeller R, Hay RJ, Hay SI, He Y, Hedayatizadeh-Omran A, Hegazy MI, Heibati B, Heidari M, Hendrie D, Henok A, Henry NJ, Herteliu C, Heydarpour F, Heydarpour P, Heydarpour S, Hibstu DT, Hoek HW, Hole MK, Homaie Rad E, Hoogar P, Hosgood HD, Hosseini SM, Hosseinzadeh M, Hostiuc M, Hostiuc S, Hotez PJ, Hoy DG, Hsiao T, Hu G, Huang JJ, Husseini A, Hussen MM, Hutfless S, Idrisov B, Ilesanmi OS, Iqbal U, Irvani SSN, Irvine CMS, Islam N, Islam SMS, Islami F, Jacobsen KH, Jahangiry L, Jahanmehr N, Jain SK, Jakovljevic M, Jalu MT, James SL, Javanbakht M, Jayatilleke AU, Jeemon P, Jenkins KJ, Jha RP, Jha V, Johnson CO, Johnson SC, Jonas JB, Joshi A, Jozwiak JJ, Jungari SB, Jurisson M, Kabir Z, Kadel R, Kahsay A, Kalani R, Karami M, Karami Matin B, Karch A, Karema C, Karimi-Sari H, Kasaeian A, Kassa DH, Kassa GM, Kassa TD, Kassebaum NJ, Katikireddi SV, Kaul A, Kazemi Z, Kazemi Karyani A, Kazi DS, Kefale AT, Keiyoro PN, Kemp GR, Kengne AP, Keren A, Kesavachandran CN, Khader YS, Khafaei B, Khafaie MA, Khajavi A, Khalid N, Khalil IA, Khan EA, Khan MS, Khan MA, Khang YH, Khater MM, Khoja AT, Khosravi A, Khosravi MH, Khubchandani J, Kiadaliri AA, Kibret GD, Kidanemariam ZT, Kiirithio DN, Kim D, Kim YE, Kim YJ, Kimokoti RW, Kinfu Y, Kisa A, Kissimova-Skarbek K, Kivimaki M, Knudsen AKS, Kocarnik JM, Kochhar S, Kokubo Y, Kolola T, Kopec JA, Koul PA, Koyanagi A, Kravchenko MA, Krishan K, Kuate Defo B, Kucuk Bicer B, Kumar GA, Kumar M, Kumar P, Kutz MJ, Kuzin I, Kyu HH, Lad DP, Lad SD, Lafranconi A, Lal DK, Lalloo R, Lallukka T, Lam JO, Lami FH, Lansingh VC, Lansky S, Larson HJ, Latifi A, Lau KMM, Lazarus VJ, Lebedev G, Lee PH, Leigh J, Leili M, Leshargie CT, Li S, Li Y, Liang J, Lim LL, Lim SS, Limenih MA, Linn S, Liu S, Liu Y, Lodha R, Lonsdale C, Lopez AD, Lorkowski S, Lotufo PA, Lozano R, Lunevicius R, Ma S, Macarayan ERK, Mackay MT, MacLachlan JH, Maddison ER, Madotto F, Magdy Abd El Razek H, Magdy Abd El Razek M, Maghavani DP, Majdan M, Majdzadeh R, Majeed A, Malekzadeh R, Malta DC, Manda AL, Mandarano-Filho LG, Manguerra H, Mansournia MA, Mapoma CC, Marami D, Maravilla JC, Marcenes W, Marczak L, Marks A, Marks GB, Martinez G, Martins-Melo FR, Martopullo I, Marz W, Marzan MB, Masci JR, Massenburg BB, Mathur MR, Mathur P, Matzopoulos R, Maulik PK, Mazidi M, McAlinden C, McGrath JJ, McKee M, McMahon BJ, Mehata S, Mehndiratta MM, Mehrotra R, Mehta KM, Mehta V, Mekonnen TC, Melese A, Melku M, Memiah PTN, Memish ZA, Mendoza W, Mengistu DT, Mengistu G, Mensah GA, Mereta ST, Meretoja A, Meretoja TJ, Mestrovic T, Mezgebe HB, Miazgowski B, Miazgowski T, Millear AI, Miller TR, Miller-Petrie MK, Mini GK, Mirabi P, Mirarefin M, Mirica A, Mirrakhimov EM, Misganaw AT, Mitiku H, Moazen B, Mohammad KA, Mohammadi M, Mohammadifard N, Mohammed MA, Mohammed S, Mohan V, Mokdad AH, Molokhia M, Monasta L, Moradi G, Moradi-Lakeh M, Moradinazar M, Moraga P, Morawska L, Velasquez IM, Morgado-Da-Costa J, Morrison SD, Moschos MM, Mouodi S, Mousavi SM, Muchie KF, Mueller UO, Mukhopadhyay S, Muller K, Mumford JE, Musa J, Musa KI, Mustafa G, Muthupandian S, Nachega JB, Nagel G, Naheed A, Nahvijou A, Naik G, Nair S, Najafi F, Naldi L, Nam HS, Nangia V, Nansseu JR, Nascimento BR, Natarajan G, Neamati N, Negoi I, Negoi RI, Neupane S, Newton CRJ, Ngalesoni FN, Ngunjiri JW, Nguyen AQ, Nguyen G, Nguyen HT, Nguyen HT, Nguyen LH, Nguyen M, Nguyen TH, Nichols E, Ningrum DNA, Nirayo YL, Nixon MR, Nolutshungu N, Nomura S, Norheim OF, Noroozi M, Norrving B, Noubiap JJ, Nouri HR,

Shiadeh MN, Nowroozi MR, Nyasulu PS, Odell CM, Ofori-Asenso R, Ogbo FA, Oh IH, Oladimeji O, Olagunju AT, Olivares PR, Olsen HE, Olusanya BO, Olusanya JO, Ong KL, Ong SKS, Oren E, Orpana HM, Ortiz A, Ortiz JR, Otstavnov SS, Overland S, Owolabi MO, Ozdemir R, Mahesh PA, Pacella R, Pakhale S, Pakhare AP, Pakpour AH, Pana A, Panda-Jonas S, Pandian JD, Parisi A, Park EK, Parry CDH, Parsian H, Patel S, Pati S, Patton GC, Paturi VR, Paulson KR, Pereira A, Pereira DM, Perico N, Pesudovs K, Petzold M, Phillips MR, Piel FB, Pigott DM, Pillay JD, Pirsaheb M, Pishgar F, Polinder S, Postma MJ, Pourshams A, Poustchi H, Pujar A, Prakash S, Prasad N, Purcell CA, Qorbani M, Quintana H, Quistberg DA, Rade KW, Anwar Rafay AR, Rahim F, Rahimi K, Rahimi-Movaghar A, Rahman M, Rahman MHU, Rahman MA, Rai RK, Rajsic S, Ram U, Ranabhat CL, Ranjan P, Rao PC, Rawaf DL, Rawaf S, Razo-Garcia C, Reddy KS, Reiner RC, Reitsma MB, Remuzzi G, Renzaho AMN, Resnikoff S, Rezaei S, Rezaeian S, Rezai MS, Riahi SM, Ribeiro ALP, Rios-Blancas MJ, Roba KT, Roberts NLS, Robinson SR, Roever L, Ronfani L, Roshandel G, Rostami A, Rothenbacher D, Roy A, Rubagotti E, Sachdev PS, Saddik B, Sadeghi E, Safari H, Safdarian M, Safi S, Safiri S, Sagar R, Sahebkar A, Sahraian MA, Salam N, Salama JS, Salamati P, De Freitas Saldanha R, Saleem Z, Salimi Y, Salvi SS, Salz I, Sambala EZ, Samy AM, Sanabria J, Dolores Sanchez-Nino M, Santomauro DF, Santos IS, Santos JV, Santric Milicevic MM, Jose BPS, Sarker AR, Sarmiento-Suarez R, Sarrafzadegan N, Sartorius B, Sarvi S, Sathian B, Satpathy M, Sawant AR, Sawhney M, Saxena S, Sayyah M, Schaeffner E, Schmidt MI, Schneider IJC, Schottker B, Schutte AE, Schwebel DC, Schwendicke F, Scott JG, Sekerija M, Sepanlou SG, Servan-Mori E, Seyedmousavi S, Shabaninejad H, Shackelford KA, Shafieesabet A, Shahbazi M, Shaheen AA, Shaikh MA, Shams-Beyranvand M, Shamsi M, Shamsizadeh M, Sharafi K, Sharif M, Sharif-Alhoseini M, Sharma R, She J, Sheikh A, Shi P, Shiferaw MS, Shigematsu M, Shiri R, Shirkoohi R, Shiue I, Shokraneh F, Shrime MG, Si S, Siabani S, Siddiqi TJ, Sigfusdottir ID, Sigurvinsdottir R, Silberberg DH, Santos Silva DA, Silva JP, Da Silva NT, Silveira DGA, Singh JA, Singh NP, Singh PK, Singh V, Sinha DN, Sliwa K, Smith M, Sobaih BH, Sobhani S, Sobngwi E, Soneji SS, Soofi M, Sorensen RJD, Soriano JB, Soyiri IN, Sposato LA, Sreeramareddy CT, Srinivasan V, Stanaway JD, Starodubov VI, Stathopoulou V, Stein DJ, Steiner C, Stewart LG, Stokes MA, Subart ML, Sudaryanto A, Sufiyan MB, Sur PJ, Sutradhar I, Sykes BL, Sylaja PN, Sylte DO, Szoeke CEI, Tabares-Seisdedos R, Tabuchi T, Tadakamadla SK, Takahashi K, Tandon N, Tassew SG, Taveira N, Tehrani-Banihashemi A, Tekalign TG, Tekle MG, Temsah MH, Temsah O, Terkawi AS, Teshale MY, Tessema B, Tessema GA, Thankappan KR, Thirunavukkarasu S, Thomas N, Thrift AG, Thurston GD, Tilahun B, To QG, Tobe-Gai R, Tonelli M, Topor-Madry R, Torre AE, Tortajada-Girbes M, Touvier M, Tovani-Palone MR, Tran BX, Tran KB, Tripathi S, Troeger CE, Truelsen TC, Truong NT, Tsadik AG, Tsoi D, Tudor Car L, Murat Tuzcu E, Tyrovolas S, Ukwaja KN, Ullah I, Undurraga EA, Updike RL, Usman MS, Uthman OA, Uzun SB, Vaduganathan M, Vaezi A, Vaidya G, Valdez PR, Varavikova E, Vasankari TJ, Venketasubramanian N, Villafaina S, Violante FS, Vladimirov SK, Vlassov V, Vollset SE, Vos T, Wagner GR, Wagnew FS, Waheed Y, Wallin MT, Walson JL, Wang Y, Wang YP, Wassie MM, Weiderpass E, Weintraub RG, Weldegebreal F, Weldegwergs KG, Werdecker A, Werkneh AA, West TE, Westerman R, Whiteford HA, Widecka J, Wilner LB, Wilson S, Winkler AS, Wiysonge CS, Wolfe CDA, Wu S, Wu YC, Wyper GMA, Xavier D, Xu G, Yadgir S, Yadollahpour A, Yahyazadeh Jabbari SH, Yakob B, Yan LL, Yano Y, Yaseri M, Yasin YJ, Yentur GK, Yeshaneh A, Yimer EM, Yip P, Yirsaw BD, Yisma E, Yonemoto N, Yonga G, Yoon SJ, Yotebieng M, Younis MZ, Yousefifard M, Yu C, Zadnik V, Zaidi Z, Zaman BS, Zamani M, Zare Z, Zeleke AJ, Zenebe ZM, Zhang AL, Zhang K, Zhou M, Zodpey S, Zuhlke LJ, Naghavi M, Murray CJL. Global, regional, and national age-sex-specific mortality for 282 causes of death in 195 countries and territories, 1980–2017: a systematic analysis for the Global Burden of Disease Study 2017. The Lancet 2018;392:1736–1788.

Sadarjoen IA, de Boer AJ, Post FH, Mynett AE. Particle Tracing in σ-Transformed Grids using Tetrahedral 6-Decomposition. 1998. pp. 71–80.

Sandoval Z. Planning and guidance of ultrasound guided High Intensity Focused Ultrasound cardiac arrhythmia therapy. Université de Rennes 1, 2015. Available from: https://www.hal.inserm.fr/tel-01241529v1

Sapareto SA, Dewey WC. Thermal dose determination in cancer therapy. International Journal of Radiation Oncology, Biology, Physics Int J Radiat Oncol Biol Phys, 1984;10:787–800.

761 Sapozhnikov OA, Pishchal'nikov YA, Morozov AV. Reconstruction of the normal velocity distribution
762 on the surface of an ultrasonic transducer from the acoustic pressure measured on an
763 reference surface. Akusticheskij Zhurnal 2003;49:416–425.

764 Schwenke M, Georgii J, Preusser T. Fast numerical simulation of focused ultrasound treatments
765 during respiratory motion with discontinuous motion boundaries. IEEE Transactions on
766 Biomedical Engineering IEEE Computer Society, 2017;64:1455–1468.

767 Soneson J. High intensity focused ultrasound simulator - File Exchange - MATLAB Central. 2015
768 [cited 2020 Apr 17]; Available from:
769 https://fr.mathworks.com/matlabcentral/fileexchange/30886-high-intensity-focused-ultrasound-
770 simulator

771 Sørensen TJ. A Method of Establishing Groups of Equal Amplitude in Plant Sociology Based on
772 Similarity of Species Content and Its Application to Analyses of the Vegetation on Danish
773 Commons. I kommissi. 1948. p. 34.

774 Tadmor E. A review of numerical methods for nonlinear partial differential equations. Bull Am Math
775 Soc 2012;49:507–554.

776 Thompson JF, Soni BK, Weatherill NP. Handbook of Grid Generation. CRC Press. 1998. p. 1136.

777 Timmis A, Townsend N, Gale C, Grobbee R, Flather M, Wilkins E, Wright L, Vos R, Bax J, Blum M,
778 Pinto F, Vardas P. European Society of Cardiology: Cardiovascular disease statistics 2017.
779 Eur Heart J 2018;39:508–577.

780 Treeby BE, Jaros J, Rendell AP, Cox BT. Modeling nonlinear ultrasound propagation in
781 heterogeneous media with power law absorption using a k-space pseudospectral method. J
782 Acoust Soc Am 2012;131:4324–4336.

783 Tung R, Vaseghi M, Frankel DS, Vergara P, Di Biase L, Nagashima K, Yu R, Vangala S, Tseng CH,
784 Choi EK, Khurshid S, Patel M, Mathuria N, Nakahara S, Tzou WS, Sauer WH, Vakil K, Tedrow
785 U, Burkhardt JD, Tholakanahalli VN, Saliaris A, Dickfeld T, Weiss JP, Bunch TJ, Reddy M,
786 Kanmanthareddy A, Callans DJ, Lakkireddy D, Natale A, Marchlinski F, Stevenson WG, Della
787 Bella P, Shivkumar K. Freedom from recurrent ventricular tachycardia after catheter ablation is
788 associated with improved survival in patients with structural heart disease: An International VT
789 Ablation Center Collaborative Group study. Heart Rhythm 2015;12:1997–2007.

790 Vyas U, Christensen D. Ultrasound beam propagation using the hybrid angular spectrum method.
791 Proceedings of the 30th Annual International Conference of the IEEE Engineering in Medicine
792 and Biology Society, EMBS'08 - "Personalized Healthcare through Technology" 2008. pp.
793 2526–2529.

794 Weinbaum S, Jiji LM, Lemons DE. Theory and Experiment for the Effect of Vascular Microstructure on
795 Surface Tissue Heat Transfer—Part I: Anatomical Foundation and Model Conceptualization. J
796 Biomech Eng 1984;106:321–330.

797 Wessapan T, Rattanadecho P. Acoustic streaming effect on flow and heat transfer in porous tissue
798 during exposure to focused ultrasound. Case Stud Therm Eng 2020;21:100670.

799 Wu Z, Kumon RE, Laughner JI, Efimov IR, Deng CX. Electrophysiological Changes Correlated with
800 Temperature Increases Induced by High-Intensity Focused Ultrasound Ablation. Ultrasound
801 Med Biol 2015;41:432–448.

802 Yuan P. Numerical analysis of an equivalent heat transfer coefficient in a porous model for simulating
803 a biological tissue in a hyperthermia therapy. Int J Heat Mass Transfer 2009;52:1734–1740.

804 Zeng X, McGough RJ. Evaluation of the angular spectrum approach for simulations of near-field
805 pressures. J Acoust Soc Am 2008;123:68–76.

806 Zhang J, Chauhan S. Fast computation of soft tissue thermal response under deformation based on
807 fast explicit dynamics finite element algorithm for surgical simulation. Comput Methods
808 Programs Biomed 2020;187:105244.

809

Figure captions list

Fig. 1. Visualization of the two grids used to describe the simulation model. (a) The reference grid corresponds to the discretization of the first frame on a heart cycle, which defines the nondeformed grid of the computation space. (b) The curvilinear grid corresponds to the displacement of reference grid centroids to their new location according to heart deformation extracted from another frame. Each frame has its specific curvilinear grid that defines the physical space, as the grid describes the real heart deformations.

Fig. 2. Description of 3D hexahedral cell geometry. In (a), the cell is described by its centroid $\mathcal{P}$, eight vertices and six faces: t, b, n, s, w and e. Each neighboring cell is described by its own centroid: top ($\mathcal{T}$), bottom ($\mathcal{B}$), north ($\mathcal{N}$), south ($\mathcal{S}$), west ($\mathcal{W}$) and east ($\mathcal{E}$). In (b), the surface vector of face e is expressed in the system coordinates base (e_1, e_2, e_3).

Fig. 3. Targeted zones in the heart: atrioventricular node (AVN) and ventricular apex (VA).

Fig. 4. Ultrasound probe: (a) Probe head photography, (b) Geometry of the HIFU transducer where all the rings are of equal-area. $Ø_{HIFU}$: diameter of the HIFU transducer; T_{HIFU}: truncation; $Ø_{hole}$: diameter of the hole for the imaging probe.

Fig. 5. Temperature (left) and thermal dose (right) distributions in the focal zone for static and mobile heart simulations in the ventricular apex (top) and the atrioventricular node (bottom) for the last computed phase of the treatment sequence.

Fig. 6. Simulation results in the VA. (a) Position of the transducer and the computation zone to target the VA in the numerical model. Temperature maps, after the last sonication, in the static heart (b) and in the moving heart (c) for temperatures > 43 °C. The three representations are the 3 planes intersecting the location of maximum temperature. The colormap is temperature (°C) between 43 and 100 °C. Thermal dose maps of the static heart (d) and the moving heart (e) simulations, with visualization of the targeted region. The first figure is a 3D representation of the lesion. The three others are the 3 planes cutting around the maximum dose. The colormap is at a power of 10 seconds, between 4.15 (14400 seconds) and 15 (10^{15} seconds).

Fig. 7. Simulation results in the AVN. (a) Position of the transducer and the computation zone to target the AVN in the numerical model. Temperature maps, after the last sonication, in the static heart (b)

838 and the moving heart (c) for temperatures > 43 °C. The three representations are the 3 planes
839 intersecting the location of maximum temperature. The colormap is in temperature (°C) between 43
840 and 100 °C. Thermal dose maps of the static heart (d) and the moving heart (e) simulations, with
841 visualization of the targeted region. The first figure is a 3D representation of the lesion. The three
842 others are the 3 planes cutting around the maximum dose. The colormap is at a power of 10 seconds,
843 between 4.15 (14400 seconds) and 15 (10^{15} seconds).

844 Fig. A.1. Schematic of the process to obtain the 4D numerical heart phantom. Raw data is composed
845 of 4D CT scans of a heart cycle, divided into 20 phases, with a spatial resolution of 0.3125^3 mm^3.
846 From the raw data, semiautomatic segmentation with ITK-snap provides a label map of different heart
847 parts (atria, ventricles, myocardium), and elastic registration with Elastix provides deformation maps at
848 each phase. A 4D heart model is constructed by combining these two results.

849 Fig. B.1. 2D representation of the relationship between the Cartesian system in the ($\mathbf{u_1}$, $\mathbf{u_2}$) basis and
850 the curvilinear system described with its covariant ($\mathbf{e_1}$, $\mathbf{e_2}$) and contravariant vectors ($\mathbf{e^1}$, $\mathbf{e^2}$). x^j are the
851 coordinates in the Cartesian system, and ξ^m are the coordinates in the covariant curvilinear system.

852 Figure C.1. Results of the convergence study. (a) Position of the voxels of interest. (b) Temperature
853 variation in two points of the mesh grid depending on the number of elements in the mesh (and
854 consequently on the spatial resolution of the computation). Each point corresponds to the temperature
855 in position 1 (left) and in position 2 (right) in degrees Celsius (°C) for different spatial resolutions in
856 mm. The two horizontal lines delimit the convergence interval, and the vertical line delimits the number
857 of elements from where the results converge.

858 **Tables**

	Heart muscle	Blood
Tissue density, ρ_t (kg.m^{-3})	1081	1050
Acoustic velocity, c (m.s^{-1})	1561	1578
Acoustic attenuation, α (dB.cm^{-1}.MHz^{-1})	0.34 (b = 1.26)	0.206 (b = 1.05)
Thermal conductivity, k_t (W.m^{-1}.°C^{-1})	0.558	0.517
Specific heat capacity, c_t (J.kg^{-1}.°C^{-1})	3686	3617
Perfusion, ω_b (kg.m^{-3}.s^{-1})	19	1160

859 Table 1. Heart and blood properties used in the HIFU treatment numerical model. (Hasgall et al. 2018)

	Ventricular apex	Atrioventricular node
Static heart	duration: 4 s volume: 29.81 mm^3	duration: 13 s volume: 30.16 mm^3
Moving heart	duration: 3.6 s volume: 29.08 mm^3	duration: 9 min volume: 29.51 mm^3

860 Table 2. Comparison of treatment duration according to the targeted region (ventricular apex or
861 atrioventricular node) and the presence or absence of motion.

Spatial resolution (mm)	0.2	0.3	0.4	0.5	0.6	0.8	1.0	1.2	1.4	1.6	1.8	2.0
Number of elements in mesh	5.7e6	1.7e6	7.1e5	3.6e5	2.1e5	8.8e4	4.6e4	2.4e4	1.6e4	1.2e4	7.6e3	5.7e3
Temperature at voxel in position 1 (°C)	66.66	65.03	67.18	47.85	55.24	41.55	49.85	40.97	45.53	37	37	37
Temperature at voxel in position 2 (°C)	59.44	59.24	59.23	64.47	52.92	41.2	64.47	41.3	44.89	51.17	45.8	53.78

862 Table C.1. Numerical results of the temperature at positions 1 and 2 depending on the spatial
863 resolution of the simulation.

(a)

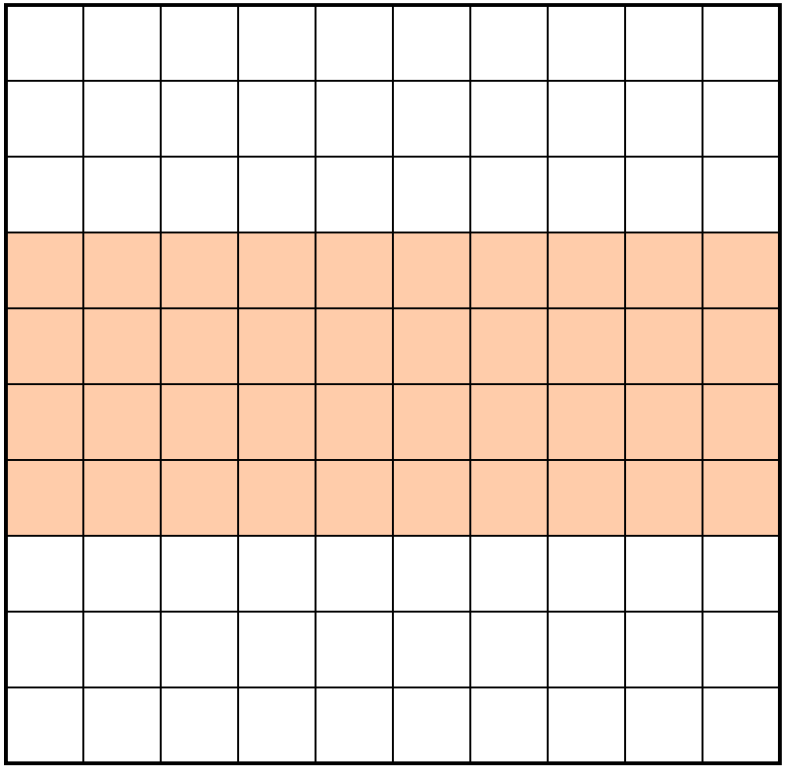

reference grid
(computation space)

(b)

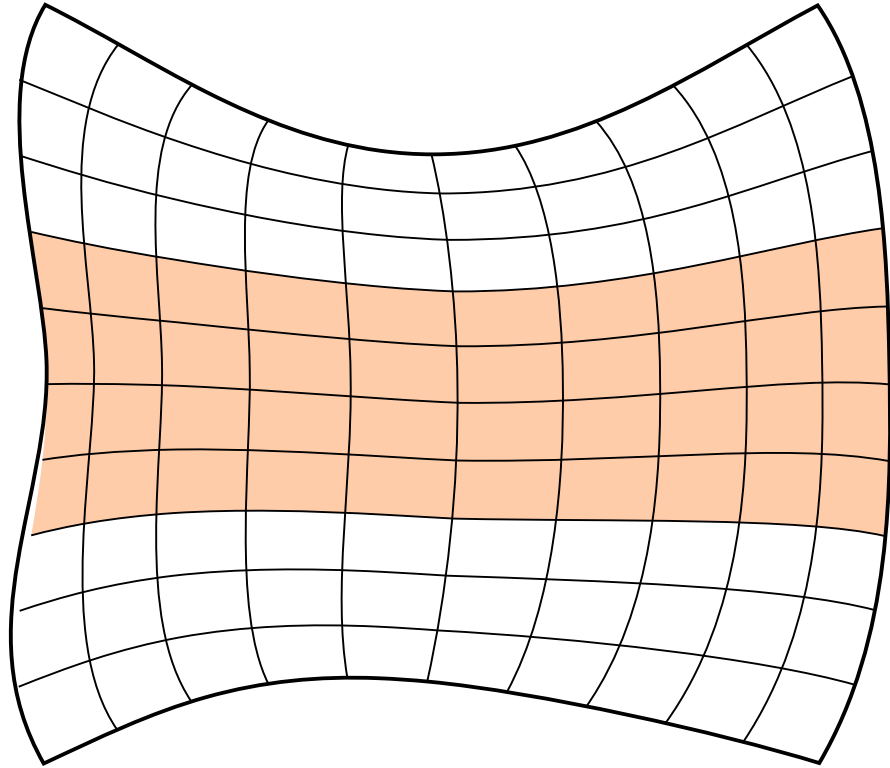

curvilinear grid
(physical space)

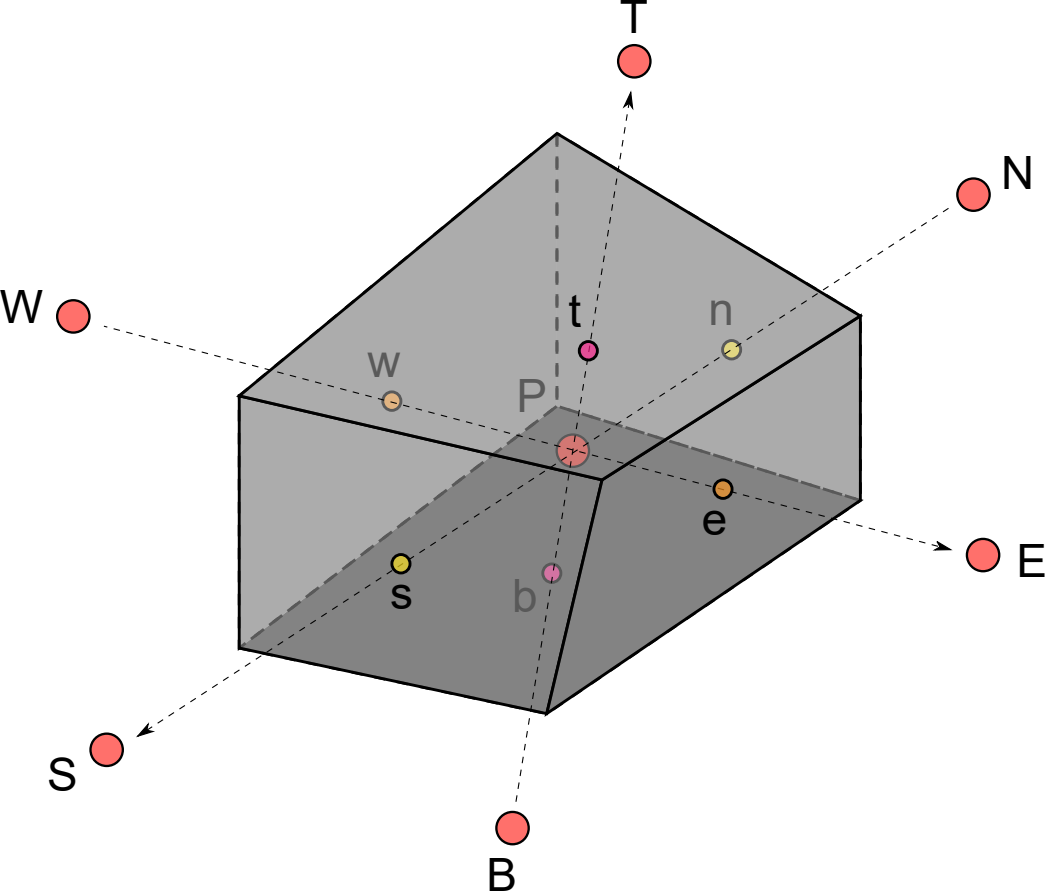
T
N
W
t
n
w
P
e
E
s
b
S
B

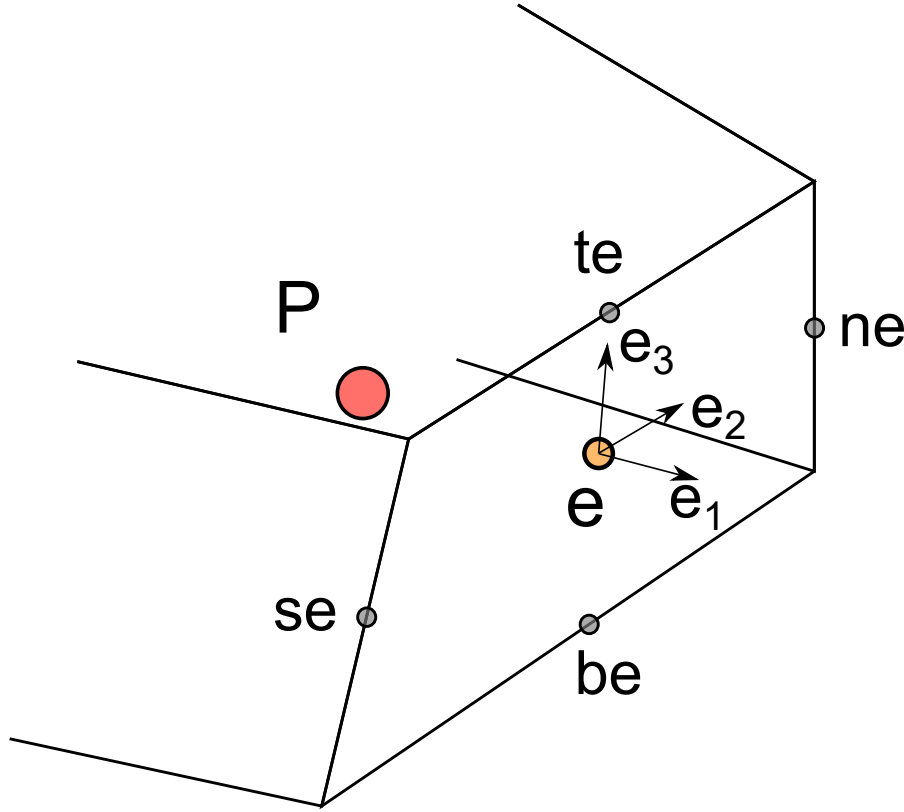
P
te
ne
e3
e2
e
e1
se
be

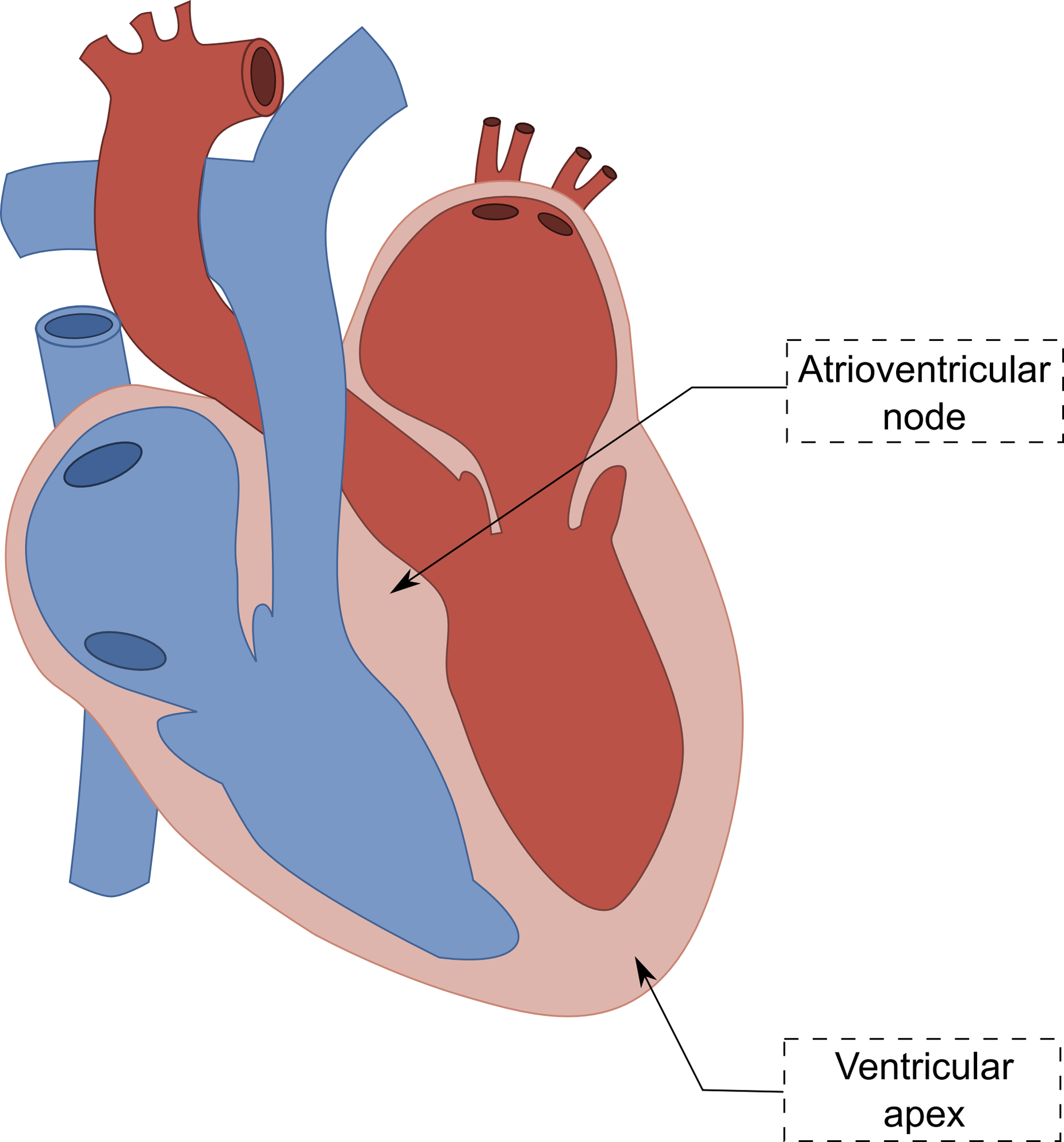
Atrioventricular node
Ventricular apex

(a)

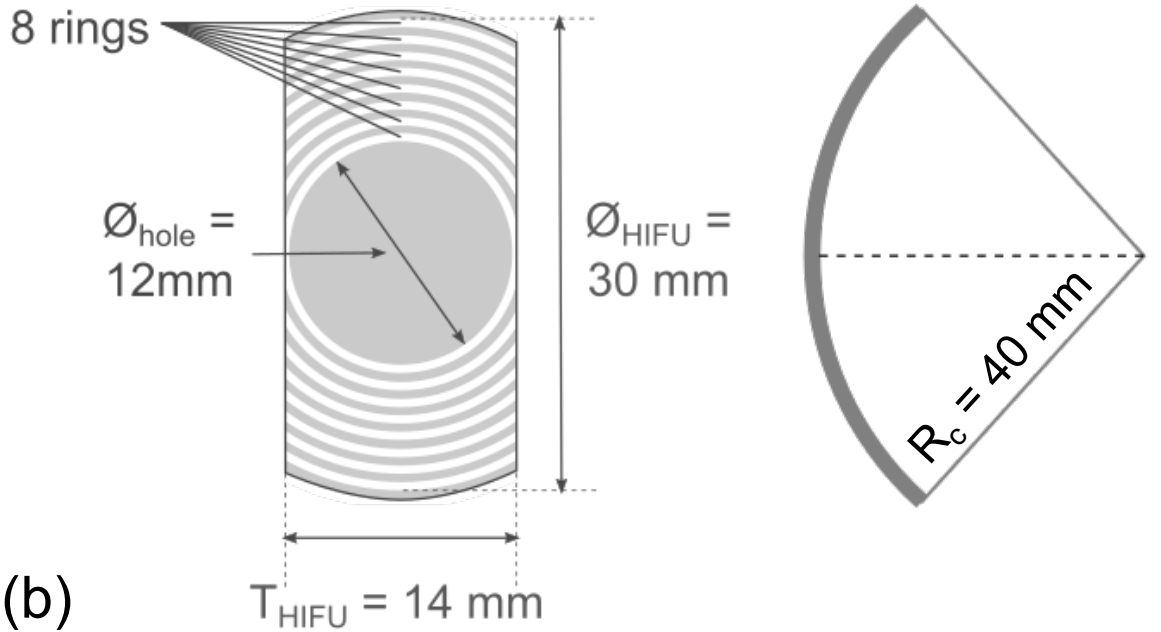

(b)

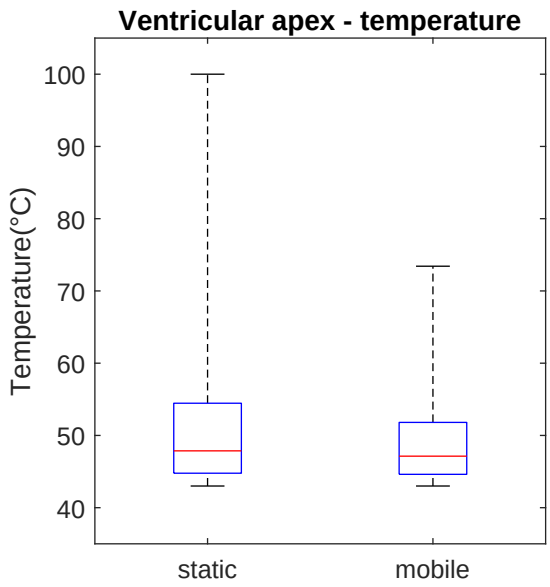
Ventricular apex - temperature
Temperature(°C)
100
90
80
70
60
50
40
static
mobile

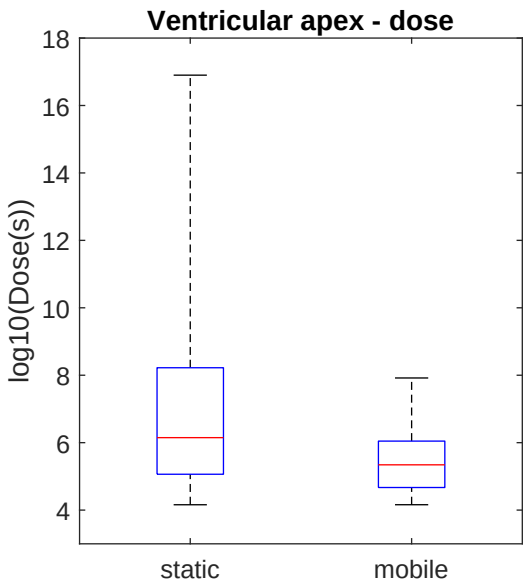
Ventricular apex - dose
log10(Dose(s))
18
16
14
12
10
8
6
4
static
mobile

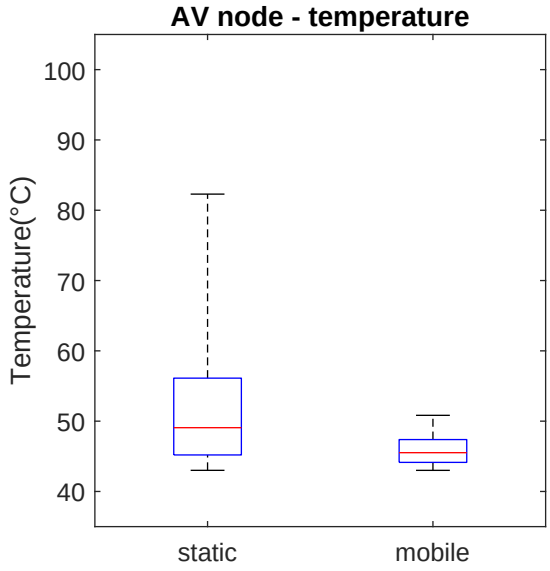
AV node - temperature
Temperature(°C)
100
90
80
70
60
50
40
static
mobile

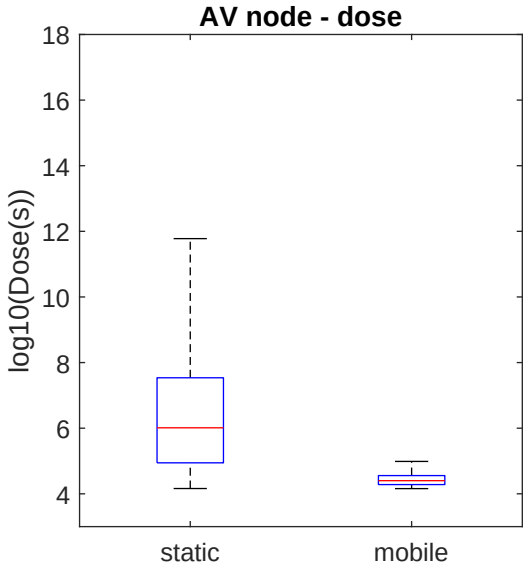
AV node - dose
log10(Dose(s))
18
16
14
12
10
8
6
4
static
mobile

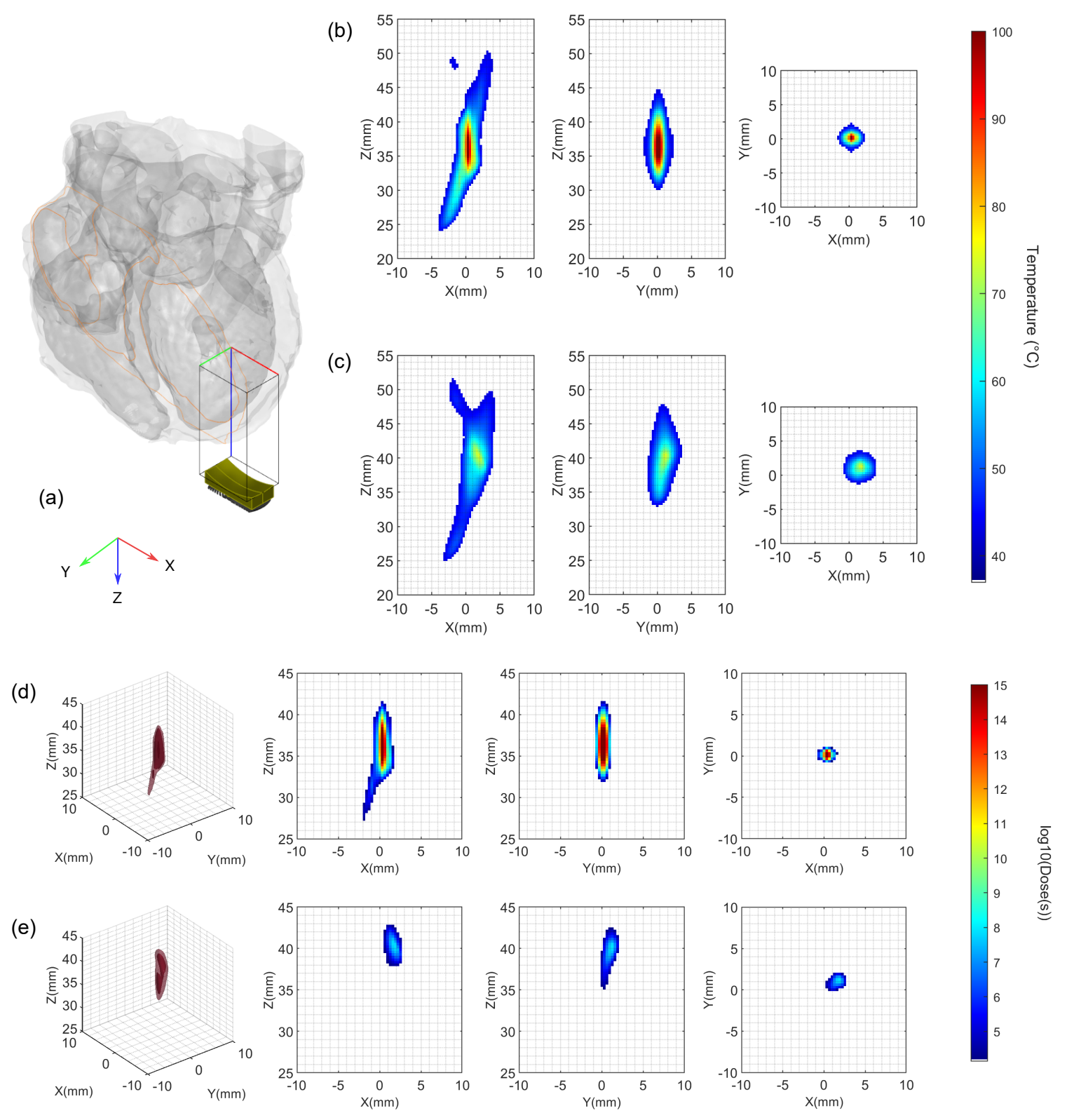
(a)
Y
X
Z
(b)
Z(mm)
X(mm)
Z(mm)
Y(mm)
Y(mm)
X(mm)
(c)
Z(mm)
X(mm)
Z(mm)
Y(mm)
Y(mm)
X(mm)
Temperature (°C)
100
90
80
70
60
50
40
(d)
Z(mm)
X(mm)
Y(mm)
Z(mm)
X(mm)
Z(mm)
Y(mm)
Y(mm)
X(mm)
(e)
Z(mm)
X(mm)
Y(mm)
Z(mm)
X(mm)
Z(mm)
Y(mm)
Y(mm)
X(mm)
log10(Dose(s))
15
14
13
12
11
10
9
8
7
6
5

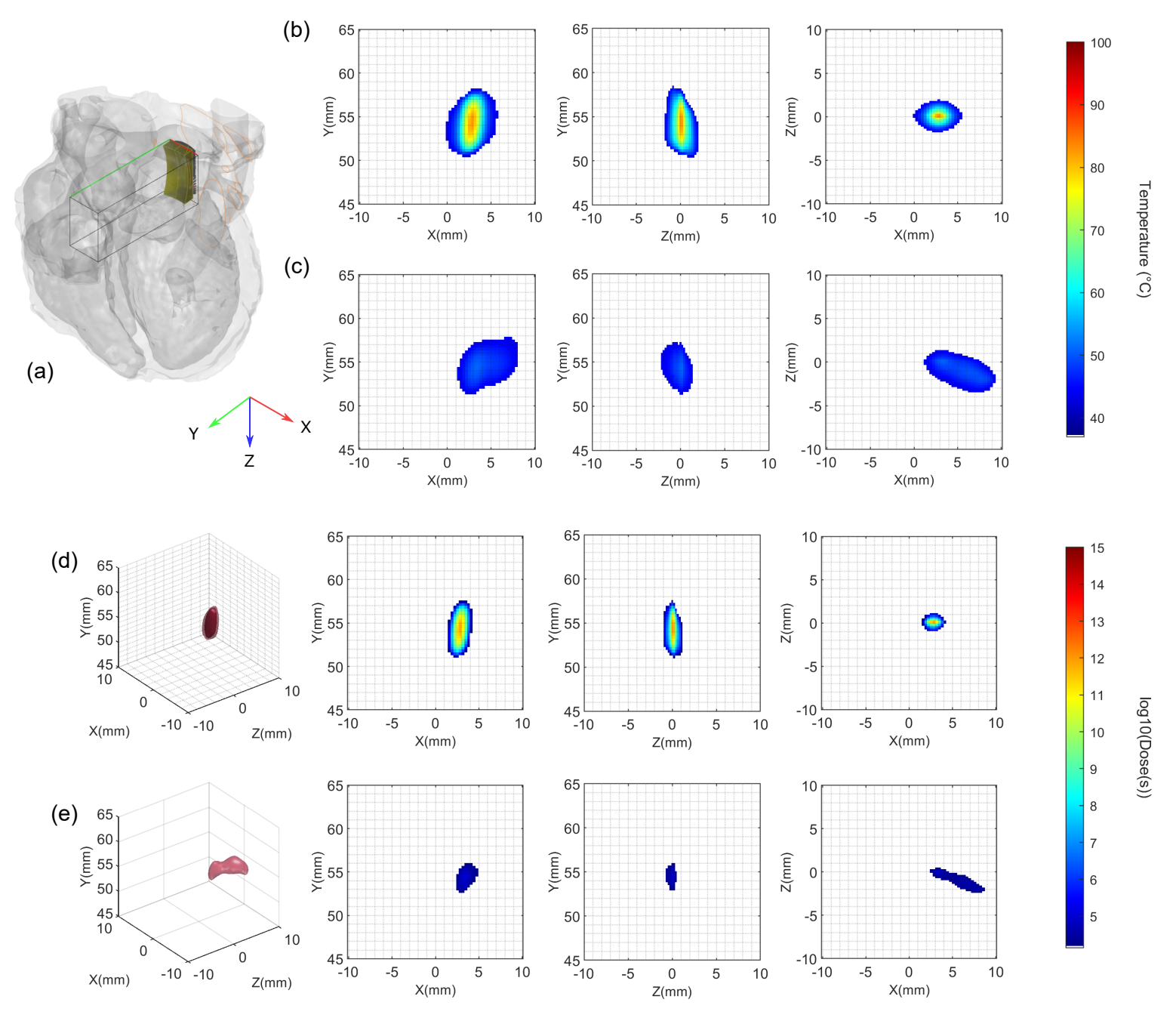
(a)
(b)
(c)
(d)
(e)
Y
X
Z
Y(mm)
X(mm)
Z(mm)
Temperature (°C)
log10(Dose(s))